Adaptive optical correction in *in vivo* two-photon fluorescence microscopy with neural fields

Iksung Kang[1,*], Hyeonggeon Kim[2], Ryan Natan[1], Qinrong Zhang[1,†], Stella X. Yu[3,4], and Na Ji[1,5,6,7,*]

[1]*Department of Neuroscience, University of California, Berkeley, CA 94720, USA*

[2]*Applied Science and Technology Graduate Program, University of California, Berkeley, CA 94720, USA*

[3]*Department of Electrical Engineering and Computer Science, University of Michigan, Ann Arbor, MI 48109, USA*

[4]*Department of Electrical Engineering and Computer Science, University of California, Berkeley, CA 94720, USA*

[5]*Department of Physics, University of California, Berkeley, CA 94720, USA*

[6]*Helen Wills Neuroscience Institute, University of California, Berkeley, CA 94720, USA*

[7]*Molecular Biophysics and Integrated Bioimaging Division, Lawrence Berkeley National Laboratory, Berkeley, CA 94720, USA*

[†]*Current address: Department of Biomedical Engineering, City University of Hong Kong, Kowloon, Hong Kong*

[*]*iksung.kang@berkeley.edu*

[*]*jina@berkeley.edu*

Abstract

Adaptive optics (AO) techniques are designed to restore ideal imaging performance by measuring and correcting aberrations originating from both the microscope system and the sample itself. Conventional AO methods require additional hardware, such as wavefront sensors and corrective devices, for aberration measurement and correction, respectively. These methods often necessitate microscopes to adhere to strict design parameters, like perfect optical conjugation, to ensure the accurate delivery of corrective patterns for wavefront correction using corrective devices. However, in general microscope systems, including commercially available ones, conjugation errors are more prone to arise due to incomplete conjugation among optical components by design and misalignment of the components, coupled with their limited access and adjustability, which hinders the rigorous integration of AO hardware. Here, we describe a general-purpose AO framework using neural fields, NeAT, that is applicable to both custom-built and commercial two-photon fluorescence microscopes and demonstrate its performance in various *in vivo* imaging settings. This framework estimates wavefront aberration from a single 3D two-photon fluorescence image stack, without requiring external datasets for training. Additionally, it addresses the issue of incomplete optical conjugation by estimating and correcting any conjugation errors, which enables more accurate aberration correction by the corrective device. Finally, it jointly recovers the sample's 3D structural information during the learning process, potentially eliminating the need for hardware-based AO correction. We first carefully assess its aberration estimation performance using a custom-built two-photon fluorescence microscope equipped with a wavefront sensor which provides the ground truth aberration for comparison. We further characterize and assess the robustness of the aberration estimation to image stacks with low signal-to-noise ratios, strong aberration, and motion artifacts. As practical applications, using a commercial microscope with a spatial light modulator, we first demonstrate NeAT's real-time aberration correction performance in *in vivo* morphological imaging of the mouse brain. We further show its performance in *in vivo* functional activity imaging of glutamate and calcium dynamics within the mouse brain.

Introduction

Fluorescence imaging of living biological organisms provides mechanistic insights into their physiology. Two-photon (2P) fluorescence microscopy is an essential tool for live imaging, probing structure and function at subcellular resolution deep within complex tissues[1]. However, as 2P excitation light propagates through tissue, its wavefront accumulates optical aberrations from refractive index mismatches, leading to reduced fluorescence signal, resolution, and contrast. When these sample-induced aberrations are measured and corrected, the excitation light can form a diffraction-limited focus, increasing fluorescence signal and improving the accuracy of structural and functional characterization.

Adaptive optics (AO)[2–5] measure aberration and correct it with wavefront-shaping devices, such as deformable mirrors (DM) and liquid-crystal spatial light modulators (SLM). AO methods[2–4,6] can be grouped into direct wavefront sensing methods, which use a wavefront sensor for aberration measurement, and indirect wavefront sensing methods, which include approaches utilizing machine learning for wavefront estimation[7–12].

Regardless of aberration measurement scheme, AO methods are generally developed for and deployed on custom-built microscopes, in which individual optical components are carefully conjugated and aligned to ensure optimal imaging and correction performance. However, microscopes in a general laboratory setting often have imperfect conjugation and misalignment of optical components, with commercial microscopes additionally suffering from limited access and adjustability of their optical paths. Furthermore, sample motion during *in vivo* imaging leads to artifacts that degrade aberration measurement accuracy, a problem that can be particularly severe for deep tissue imaging as well as for indirect wavefront sensing methods that utilize serial measurement of images and signals[4].

Here, we describe NeAT, **Ne**ural fields for **A**daptive optical **T**wo-photon fluorescence microscopy. It utilizes neural fields to present the sample's 3D structure and incorporates additional computational architectures to enhance AO performance for imperfect microscopes and living samples. By incorporating a physics prior, specifically, an image-formation model for two-photon fluorescence microscopy that accounts for both aberration and sample motion, NeAT estimates aberrations from a single fluorescence image stack without requiring external datasets for training, even in the presence of motion artifacts. NeAT also corrects for conjugation errors in the microscope system, ensuring that a corrective phase pattern displayed on a wavefront-shaping

device accurately cancels out aberration even after propagation through imperfectly conjugated and misaligned optics. Lastly, NeAT jointly recovers the sample's 3D structure with aberration. In scenarios where additional imaging with aberration correction is not needed, NeAT eliminates the need for corrective devices, further reducing system cost and complexity.

The paper is structured as follows. First, we implement NeAT in a perfectly conjugated 2P fluorescence microscope equipped with a wavefront sensor capable of direct wavefront sensing (DWS). We then compare the performance of NeAT with the ground-truth aberration correction from DWS in both *in vitro* and *in vivo* scenarios, and determine the performance limits in terms of signal-to-noise ratio (SNR) and aberration severity. Next, we implement NeAT in a commercial microscope with imperfect conjugation and evaluate its real-time aberration correction performance for *in vivo* 3D morphological and functional imaging within the living mouse brain.

Results

NeAT, a general-purpose AO framework in 2P fluorescence microscopy using neural fields

NeAT is designed to jointly estimate wavefront aberration and recover the sample's 3D structural information from an input 3D image stack. It utilizes neural fields – implicit functions represented by a coordinate-based neural network across spatial coordinates[14] – to represent sample structure. NeAT also incorporates a mathematical image-formation model for 2P fluorescence microscopy into the learning process, which involves aberration and structural estimation, as well as motion correction through learnable image transformations. During the learning process, NeAT aims to reproduce an image stack closely resembling the input by iteratively adjusting its parameters. This process requires no external supervision.

The input for NeAT is an image stack (g) acquired through *z*-axis scanning (**Fig. 1a**). Artifacts caused by sample motion (e.g., body movement, breathing, and heartbeat) in the *z* stack, if present, are corrected by a set of affine transformations (A) whose parameters are optimized during the learning process (**Fig. 1b**, **Fig. S1c**). In the absence of motion artifacts, A is set as an identity operator and excluded from the learnable parameters.

The image-formation model consists of three components: point spread function (PSF, h), structure (s), and baseline (b). The PSF h is computed as[15]:

$$h(\boldsymbol{r};\alpha) = \left| \mathcal{F}\left\{ P(u,v)\, e^{i\varphi(u,v;\alpha)}\, e^{-2\pi i z\sqrt{k_0^2-u^2-v^2}} \right\} \right|^4. \quad (1)$$

Here, $\boldsymbol{r}$ represents the spatial coordinates (x, y, z) near the focal plane. $P(u,v)$ and $\varphi(u,v;\alpha)$ stand for the amplitude and phase maps in the coordinates (u,v) within the circular pupil of the objective lens, respectively. $\varphi(u,v;\alpha)$ is a linear combination of Zernike modes with their associated coefficients α, with $\varphi(u,v;\alpha) = \sum_{|m|\le 3}\sum_{n=2}^{4} \alpha_n^m Z_n^m(u,v)$. Here m and n stand for the angular meridional frequency and radial order, respectively, following the American National Standards Institute (ANSI) standard convention. We only consider the modes with $2 \le n \le 4$ and $|m| \le 3$, resulting in 10 Zernike modes to be learned, as we observed that including higher-order modes leads to inaccurate aberration estimation. The 1D tensor α are learned Zernike coefficients (**Fig. S1b**).

Next, the 3D structure *s* is rendered by a neural field (**Fig. S1a**). It involves both the spatial encoding in the Fourier domain[16,17] and a multi-layer perceptron[13,18] and receives the spatial coordinates $\boldsymbol{r}$ as input. *s* is parametrized by the network weights θ and referred to as $f_\theta(\boldsymbol{r})$.

The baseline term (*b*, **Fig. S1d**) is modeled as the multiplication of three 2D tensors that represent baseline elements along each of the *x*, *y*, and *z* axes. This term accounts for both the offset due to background fluorescence and noise and, if present, the signal decrease along the *z* axis due to scattering and absorption by tissue.

The image-formation model computes an image stack $\hat{g}$ from PSF $h(\boldsymbol{r};\alpha)$, structure $s = f_\theta(\boldsymbol{r})$, and baseline $b(\boldsymbol{r})$ by convolving PSF and structure before summation with baseline:

$$\hat{g}(\boldsymbol{r}) = f_\theta(\boldsymbol{r}) \circledast h(\boldsymbol{r};\alpha) + b(\boldsymbol{r}). \tag{2}$$

NeAT then compares the input stack g (or with motion correction, Ag) and the computed stack $\hat{g}$, running an optimization process to update the parameters over iterations (**Fig. 1c**). The optimization is performed toward minimizing the loss function (**Fig. S1e**):

$$\theta^*, \alpha^*, A^* = \underset{\theta,\alpha,A}{\operatorname{argmin}} \left(\mathcal{L}(Ag, \hat{g}) + \mathcal{R}(s)\right). \tag{3}$$

The fidelity term $\mathcal{L}(Ag, \hat{g})$ is a convex combination of SSIM (Structural Similarity Index Metric)[19] and rMSE (relative Mean-Squared Error)[20–22] between the two stacks, where SSIM measures the similarity between Ag and $\hat{g}$ and rMSE computes a weighted L2 loss that reduces the influence of bright pixels and places greater emphasis on minimizing errors in dark regions. The regularization term $\mathcal{R}(s)$ incorporates a generic prior on the spatial piecewise smoothness of the structure and is the summation of three regularizations based on second-order total variation[23,24], L1, and nonlinear diffusion[25]. Second-order total variation and L1 regularizations are chosen for rendering spatially sparse structural features (e.g., sparsely labeled neurons). Nonlinear diffusion regularization is employed to avoid both low-frequency and high-frequency artifacts in the structure recovered by NeAT. More detailed information about the image-formation model, loss function, and regularization is available in **Methods**.

Performance validation with DWS-AO

To evaluate the accuracy of NeAT's aberration estimation, we compared the aberration output by NeAT with the ground-truth aberration from DWS with a Shack-Hartmann wavefront sensor, using a custom-built 2P microscope with perfect conjugation between optics, including between

the X and Y galvos (**Fig. S2a**). Microscope system aberration was measured with DWS and corrected by a DM prior to all experiments.

We first validated NeAT's performance using 2P imaging of fixed Thy1-GFP line M transgenic mouse brain slices. A #1.5 coverslip was placed above a brain slice at a 3° tilt, which introduced aberrations similar to those typically induced by a cranial window during *in vivo* mouse brain imaging[26]. We set the correction collar of the objective lens to 0.17, the nominal thickness of the coverslip. From an input image stack (**Fig. 2a**), NeAT output 3D neuronal structure whose lateral (*xy*) and axial (*xz*) maximal intensity projections (MIPs) showed neuronal processes as well as synaptic structures such as boutons and dendritic spines (**Fig. 2b**). The estimated aberration had a similar phase map to the DWS measurement with a root mean square (RMS) difference of 0.09 wave (**Fig. 2c**) and comparable coefficients in the dominant aberration modes, e.g., primary coma $Z_3^{\pm 1}$ (**Fig. 2d**).

Next, we applied NeAT to *in vivo* 2P imaging of the mouse brain cortex. In one mouse, breathing caused lateral shifts between images at different *z* (**Fig. 2e**). Without correcting for these motion artifacts, the algorithm misinterpreted the laterally displaced images of the same structure at different *z* as separate structures, leading to striated appearance in the axial MIP of its structural output (**Fig. 2f**). NeAT addressed this by using affine transformations to register the image stack, with the transformation matrices jointly learned alongside other parameters (**Eq. 3**). With sample motion corrected, the structural output was free of striation artifacts (**Fig. 2g**), and the aberration output much more closely resembled the ground truth (an RMS error of 0.07 wave) than the output without motion correction (an RMS error of 0.16 wave) (**Fig. 2h,i**).

The effectiveness of sample motion correction depends on the SNR of fluorescence images and the magnitude of sample motion (**Fig. S3**). For high SNR images (e.g., SNR of 12), NeAT could handle sample motions of ± 2 μm of maximum displacement. For noisy images (e.g., SNR of 3), its accuracy decreased and can only handle sample motions with < 0.5 μm displacement. This finding offers practical guidance for controlling anesthesia level to minimize sample motion during image acquisition for AO, particularly during deep tissue imaging when SNR is low.

Performance limit characterizations

After validating NeAT's performance both *in vitro* and *in vivo*, we evaluated how robust it performed at varying SNR levels. We varied post-objective power and acquired image stacks of

1-μm-diameter fluorescence beads at different SNRs with primary astigmatism (Z_2^{-2}, **Fig. S4a**) or primary coma (Z_3^{-1}, **Fig. S4b**) introduced to the DM. At low SNR levels (e.g., SNR < 1.5), fluorescent beads were poorly visualized and the structures output by NeAT appeared fragmented as they were fitted to noise. Only at sufficiently high SNRs did the structure resemble beads (**Fig. S4a, b**). We quantitatively evaluated NeAT's performance to identify the cutoff SNR below which NeAT's performance deteriorated abruptly[27]. We computed the Pearson correlation coefficient (PCC) between the recovered structures at different SNRs and that from an image stack acquired with no aberration and high SNR (SNR > 7, **Fig. S4a, b**). By fitting the PCC values to a piecewise linear curve with two distinct slopes, we identified the cutoff SNR as 1.94 for astigmatism (**Fig. 2j**) and 1.56 for coma (**Fig. 2k**). Below the cutoff SNRs, the accuracy of structural recovery decreased, as indicated by an abrupt drop of PCC values (blue curve, **Fig. 2j,k**); The accuracy of aberration estimation also decreased, as indicated by an increase in wavefront error (quantified by the RMS error between NeAT estimate and ground-truth aberrations; green curve, **Fig. 2j,k**).

We repeated the experiment on a fixed Thy1-GFP line M mouse brain slice to determine whether similar limits applied to spatially extended biological structures. In this case, we applied primary coma (Z_3^{-1}, **Fig. S4c**) and secondary astigmatism (Z_4^{-2}, **Fig. S4d**) to the DM separately. Similarly to beads, low-SNR images were associated with structures dominated with artifacts (**Fig. S4c, d**). As before, we calculated the PCC between the recovered structures at different SNRs and the ground truth from an image stack acquired with no aberration and high SNR (SNR > 5, **Fig. S4c, d**). We found that the cutoff SNR was 1.90 for coma (**Fig. 2m**) and 1.53 for astigmatism (**Fig. 2n**), similar to the cutoff SNRs from the bead data. This suggests that at sufficiently high SNRs (SNR > 2 for aberrations tested here), NeAT achieves accurate structural recovery, independent of feature characteristics.

Moreover, we characterized NeAT's performance limit in terms of aberration severity. We randomly generated Zernike coefficients to obtain mixed-mode aberrations with RMS values ranging from 0.05 to 0.65 waves. We then applied each aberration to the DM and acquired images of beads and brain slices at SNR > 8. With the increase of aberration, fluorescence images became more degraded in resolution and contrast (**Fig. S5**). At the largest aberrations tested (e.g., 0.65 waves for beads and 0.43 waves for brain slices), the recovered structures no longer accurately represented the features of the beads or neurons. We computed the PCC between the structures retrieved by NeAT from images with varying levels of external aberration and the structure from

an image stack without aberration. Similar to above, we defined the cutoff RMS as the value above which the PCC exhibited a sudden drop, as identified by fitting the PCC values to a piecewise linear curve with two distinct slopes. We found a cutoff RMS of 0.56 wave for 1-μm beads (**Fig. 2n**) and 0.36 wave for the brain slice (**Fig. 2o**), respectively. This difference in cutoff RMS values is expected as 3D extended structures generally pose greater challenges than beads.

Lastly, we characterized NeAT's performance limit in terms of sampling rate by varying the pixel sizes of input image stacks. We downsampled both *in vitro* and *in vivo* image stacks of mouse neurons by different factors to control the input pixel size along the lateral (*dx, dy*) and axial (*dz*) axes, and compared NeAT's performance in structural recovery and aberration estimation (**Fig. S6, 7**). When pixel size exceeded the Nyquist sampling criterion, the structure outputs from NeAT became inaccurate. The aberration estimation also deviated from the ground truth measured by DWS, with the estimated aberration matching the DWS measurement until the lateral pixel size exceeded 0.20 μm and axial pixel size exceeded 0.67 μm, values dictated by the Nyquist condition, for both *in vitro* (**Fig. S6a**, **Fig. S7a**) and *in vivo* (**Fig. S6b**, **Fig. S7a**) cases.

NeAT corrects for conjugation errors in a commercial microscope

Having demonstrated the successful application of NeAT in a custom-built 2P fluorescence microscope and acquired a thorough understanding of its performance in relation to SNR, aberration severity, and input pixel size, we next tested whether NeAT worked on a commercial 2P microscope. This was motivated by the desire to expand the application of AO beyond optical specialists to a general laboratory setting with microscopes having imperfect conjugation and misalignment of optical components, as well as limited access and adjustability of their optical paths.

We added a liquid-crystal SLM to the beam path between an excitation laser and a commercial 2P fluorescence microscope (Bergamo II, Thorlabs) (**Fig. S2b**). This system differs from our custom-built microscope in several ways. First, the DM, *x* galvo, and *y* galvo of the custom-built system were conjugated with pairs of lenses (**Fig. S2a**) to ensures that the corrective phase pattern displayed on the DM was accurately relayed to the back focal plane (BFP) of the objective lens and stayed stationary during beam scanning. But the commercial microscope, as typical for microscopes in biological laboratories, did not conjugate the two galvos but placed them close to each other. Second, while the optics of the custom-built system were carefully

arranged and aligned to ensure the registration between the x and y axes of the SLM surface and the fluorescence images, the commercial microscope had multiple mirrors in an enclosed optical path whose placement and alignment were preset and not adjustable. Finally, the commercial system was designed to have the whole microscope body move in 3D to accommodate large samples, which causes alignment errors between the SLM on the optical table and the objective lens in the microscope that for heavily shared microscope can vary daily. As a result, a wavefront applied to the corrective device is translated, rotated, scaled, and/or sheared at the BFP of the objective lens of the commercial microscope, which in turn degrades the performance of aberration correction.

To address this problem, we incorporated into NeAT a process to estimate and correct conjugation errors of commercial microscopes. Corrective wavefront displayed on the SLM, φ_{Corr}, becomes φ_{BFP} at the BFP of the objective lens, with

$$\varphi_{\mathrm{BFP}} = H\varphi_{\mathrm{Corr}} + \Phi_{\mathrm{Sys}} \tag{4}$$

Here Φ_{Sys} represents the system aberration and H is a linear geometric transformation describing the effects of conjugation errors on φ_{Corr} (**Fig. 3a**). We model H as an affine transformation with parameters for translational, rotational, scaling, and shear transformation (**Fig. 3b**). For microscopes with perfect conjugation, $H = I$, the identity operator (*i.e.* translations are 0 pixels in x and y, rotation is 0 deg, scaling is 1, and shear is 0). For microscopes with conjugation errors, the process of accounting for them requires finding the transformation H and system aberration Φ_{Sys}.

We determine system aberration Φ_{Sys} by inputting into NeAT an image stack of 200-nm-diameter fluorescence beads acquired with a flat phase pattern applied to the SLM. The estimated system aberration from NeAT is $\hat{\phi}_0$, with

$$\Phi_{\mathrm{Sys}} = \hat{\phi}_0 + \varepsilon_0 \tag{5}$$

Here ε_0 represents estimation error by NeAT, which should be much smaller in RMS magnitude than Φ_{Sys}.

To determine H, we apply 5 calibration aberrations Φ_n (n = 1 to 5) that allow us to detect translation, scaling, rotation, and shear errors, including primary astigmatism (Z_2^{-2} and Z_2^2), coma (Z_3^{-1} and Z_3^1), and spherical aberration (Z_4^0), to the SLM. At the objective lens BFP, these

aberrations became $H\Phi_n + \Phi_{\text{Sys}}$. With image stacks of 200-nm fluorescence beads acquired under these external aberrations as inputs (**Fig. 3c**), NeAT returns $\hat{\phi}_n$ (n = 1 to 5), with

$$H\Phi_n + \Phi_{\text{Sys}} = \hat{\phi}_n + \varepsilon_n \tag{6}$$

Here ε_n represents estimation error by NeAT. Subtracting (5) from (6) and assuming $\varepsilon_n - \varepsilon_0 \approx 0$, we have

$$H\Phi_n \cong \hat{\phi}_n - \hat{\phi}_0, \qquad n = 1,2,\dots,5 \tag{7}$$

Now with Φ_n (n = 1 to 5) known, and $\hat{\phi}_n$ and $\hat{\phi}_0$ from NeAT, we determine the parameters of H by minimizing the loss function:

$$\hat{H} = \underset{H}{\text{argmin}} \left(\sum_{n=1}^{5} \left| H\Phi_n - \left(\hat{\phi}_n - \hat{\phi}_0\right) \right| \right) \tag{8}$$

$\hat{H}$, the estimate for H, describes how the conjugation errors in the system translate, rotate, scale, and shear the wavefront pattern applied to the SLM on its way to the BFP of the objective lens. To correct these errors, we then apply the inverse of $\hat{H}$, $\hat{H}^{-1}$, to the aberration estimation $\hat{\phi}$ from NeAT and use $\hat{H}^{-1}\hat{\phi}$ as the corrective pattern on the SLM (**Fig. 1d**).

For example, to correct for system aberration of the commercial microscope, we used an image stack of 200-nm fluorescence beads as input to NeAT, which returned $\hat{\phi}_0$ as the aberration estimation. Directly applying $\hat{\phi}_0$ to the SLM increased the signal of a fluorescent bead by 1.7-fold ("AO1, w/o H", **Fig. 3d,e**). By also correcting for conjugation errors, $\hat{H}^{-1}\hat{\phi}_0$ increased the signal by 2.2-fold ("AO1, w/ H", **Fig. 3d,e**). Using the image stack acquired with $\hat{H}^{-1}\hat{\phi}_0$ as input into NeAT, we obtained the residual aberration $\hat{\phi}_0'$ and applied $\hat{H}^{-1}\left(\hat{\phi}_0 + \hat{\phi}_0'\right)$ to the SLM, leading to a 3.0-fold signal gain over no aberration correction ("AO2, w/ H", **Fig. 3d,e**). From the image stacks acquired with these corrective patterns, NeAT estimated the residual aberrations. Consistent with the fluorescent signal measurements, conjugation error correction substantially reduced residual aberration, with 0.14 and 0.12 wave RMS after first and second iterations of AO correction, while the residual aberration without conjugation correction had a 0.22 wave RMS (**Fig. 3f**).

We further tested our approach on correcting known astigmatism, coma, and spherical aberrations introduced to the SLM. From bead image stacks acquired with these aberrations applied, NeAT returned estimated aberrations ("Estimated w/o H", **Fig. 3g**), which represented the

wavefront distortion at the objective BPF and substantially differed from the applied aberrations ("Applied aberration", **Fig. 3g**) due to conjugation errors. Transforming the estimated aberration with $\widehat{H}^{-1}$, we obtained aberrations with phase maps ("Estimated w/ H", **Fig. 3g**) that closely matched the given aberrations in all three cases, leading to much smaller RMS errors (astigmatism: 0.087 and 0.19 wave RMS with and without *H* corr; coma: 0.14 and 0.19 wave RMS with and without *H* corr; spherical: 0.16 and 0.23 wave RMS with and without *H* corr). Once characterized, the same $\widehat{H}^{-1}$ can be applied as long as the conjugation of the microscope remains unchanged. Below, the system aberration of the commercial microscope was always corrected for "No AO" images so that improvement by AO arose from the correction of sample-induced aberrations.

Real-time aberration correction for *in vivo* structural imaging of mouse brain

We evaluated NeAT's capacity to improve *in vivo* structural imaging of the commercial microscope. We acquired an image stack of a tdTomato-expressing dendrite at 350 μm depth in the primary visual cortex (V1) of a head-fixed awake mouse ("No AO", **Fig. 4a**) and used it as input to NeAT. Applying to the SLM the corrective wavefront from NeAT with both motion and conjugation corrections, we imaged the same dendrite and observed a marked improvement in brightness (up to 1.8× for dendritic spines), resolution, and contrast ("Full correction", **Fig. 4a**).

Correcting for both sample motion and conjugation error was necessary for the observed improvement. The corrective wavefront with only motion correction but not conjugation correction substantially differed from that with full correction (**Fig. 4b**) and led to more modest improvements in image quality ("Without H", **Fig. 4a**). Only correcting for conjugation but not motion similarly underperformed ("Without motion correction", **Fig. 4a**), as shown quantitatively in the lateral and axial intensity profiles of three dendritic spines (**Fig. 4c**).

We investigated further whether image-registration software such as the StackReg plugin in ImageJ can work similarly well to the motion correction method integrated into the learning process of NeAT. We acquired an image stack of beads with aberration, introduced simulated motion artifacts, pre-registered the stack with StackReg, and then used the resulting image stack as input to NeAT. Although structural recovery was moderately successful for beads (**Fig. S8a, b**), the accuracy of aberration estimation from the pre-registered image stack was inferior to inputting the un-registered stack to NeAT directly (**Fig. S8c**). Similarly, pre-registration with StackReg on an image stack acquired *in vivo* led to a corrective wavefront with smaller brightness improvement

than the corrective wavefront from motion correction by NeAT (**Fig. S8d,e**). This can be explained by whether motion correction considers the existence of aberration. While NeAT integrates motion correction into its learning process for aberration (**Eq. 3**), conventional image registration is unaware of aberrations and matches features between adjacent image planes to align them, which may inadvertently reduce or exaggerate certain aberrations (e.g., the axially curved tail of comatic aberration may be straightened by StackReg).

Having established that both conjugation and motion corrections are needed for *in vivo* imaging using the commercial microscope, we further tested NeAT's performance for morphological imaging in the awake brain of a Thy1-GFP line M mouse deep into layer 5 (L5) of V1. We first used an image stack acquired at a depth of 280 μm as input to NeAT ("No AO", **Fig. 4d**) to obtain the corrective wavefront (**Fig. 4e**, 0.36 wave RMS,), which led to resolution improvement as well as an ~2× increase in spine brightness ("AO", **Figs. 4d**,**f**). We then acquired an image stack at 500 μm depth while applying to the SLM the corrective wavefront at 280 μm ("$AO_{280\,\mu m}$", **Fig. 4g**). Using the image stack as input to NeAT, we obtained a corrective wavefront, which was then added to the corrective wavefront at 280 μm to obtain the final corrective pattern (**Fig. 4h**, 0.49 wave RMS). This corrective wavefront has a larger RMS magnitude than that at 280 μm, consistent with previous observation of stronger aberrations at larger imaging depth for the mouse brain[28]. Compared to the image stacks acquired without AO ("No AO", **Fig. 4g**) and with corrective wavefront at 280 μm ("$AO_{280\,\mu m}$", **Fig. 4g**), images after correction at 500 μm ("$AO_{500\,\mu m}$", **Fig. 4g**) showed the largest improvement in resolution and brightness, with up to a 2.4-fold increase in brightness for dendritic and synaptic structures (**Fig. 4i**). Here by using the corrective wavefront at a shallower depth when acquiring the input image stack at a deeper depth, we overcame the limit on aberration severity and used NeAT to correct large aberrations experienced in deep tissue imaging.

NeAT improves *in vivo* glutamate imaging from the mouse brain

We next used NeAT with motion and conjugation correction to improve *in vivo* functional imaging in head-fixed mice under light anesthesia (0.5% isoflurane in O2). We expressed the genetically encoded glutamate indicator iGluSnFR3[29] sparsely in V1 neurons (**Methods**). From an image stack of dendrites at 400-μm depth (**Fig. 5a**), NeAT returned a corrective wavefront (**Fig. 5b**) that substantially increased image resolution and contrast, resulting in approximately two-fold

improvement in brightness as shown by axial profiles of dendritic spines (i,ii; **Fig. 5c**) and a lateral profile across a dendritic spine and its nearby dendrite (iii; **Fig. 5c**).

Subsequently, we presented gratings drifting in eight different directions ($0°, 45°, \cdots, 315°$; 10 repetitions) to the mouse and recorded time-lapse images of the dendritic spines in the same FOV as in **Fig. 5a**, with and without aberration correction at a 60 Hz frame rate. With iGluSnFR3 labeling, changes in fluorescence brightness reflected glutamate release and thus synaptic input strength at these dendritic spines. Consistent with the above result, AO increased the brightness of dendrites and spines in the averaged time-lapse image (**Fig. 5d**; **Fig. 5e**, zoomed-in views of white boxes in **Fig. 5d**). For four dendritic spines (ROI 1-4, **Fig. 5e**), AO correction doubled the basal intensity (F_0) of their trial-averaged fluorescent traces and led to more prominent glutamate transients with larger amplitudes ($\Delta F/F_0$) (left and middle panels, **Fig. 5f**). Fitting the glutamate responses to the 8 drifting grating stimuli with a bimodal Gaussian curve[30], we obtained the orientation-tuning curves for these spines (right panels, **Fig. 5f**). Here AO increased the response amplitudes to the preferred grating orientations and led to a higher orientation sensitivity index (OSI) for these spines. Correcting aberration also shifted the preferred orientation of some spines, resulting in more similar tuning preference for neighboring spines (**Fig. 5g**), consistent with previous findings[31]. Consistently across dendritic spine populations (52 orientation-sensitive ROIs out of 86 (60%), **Methods**), aberration correction by NeAT significantly increased basal fluorescence F_0 (two-sided paired t-test, $p < 0.001$, **Fig. 5h**). It also increased $\Delta F/F_0$ and OSI values as indicated by pairwise comparison (two-sided paired t-test, $p < 0.001$, **Fig. 5i** and **Fig. 5j**, respectively) and the cumulative OSI distributions (Kolmogorov-Smirnov test, $p < 0.001$, **Fig. 5k**).

NeAT improves *in vivo* calcium imaging in densely labeled brains

We further demonstrated that NeAT can also be applied to densely labeled brains, a common application scenario for *in vivo* calcium imaging of neuronal populations. As NeAT requires an input stack of sparse structures for aberration estimation, we used viral transduction to densely express the genetically encoded calcium indicator GCaMP6s[32] and sparsely expressed the red fluorescent protein tdTomato in L2/3 neurons of the mouse V1 (**Methods**). Because aberration estimation and correction can be performed at different excitation wavelengths without compromising correction performance (**Fig. S9**), we used an image stack of a tdTomato-expressing neuron (inside yellow box of **Fig. 5l**) acquired with 1000 nm excitation light as the input to NeAT

($32\times32\times10$ μm^3 stack, "No AO", **Fig. 5m**) to obtain the corrective wavefront (**Fig. 5n**). AO visibly improved image contrast and resolution of the tdTomato-expressing neuron ("AO", **Fig. 5m**), leading to a >2× increase in intensity in both axial profiles at dendritic spines and lateral profiles across dendrites (**Fig. 5o**).

Next, we switched the excitation wavelength to 920 nm and acquired images of GCaMP6s-expressing neurons over a 484×484 μm^2 FOV (green channel of **Fig. 5l**) without and with the corrective wavefront obtained by NeAT from the tdTomato-expressing neuron at 15 Hz, while presenting drifting gratings to the head-fixed mouse under light anesthesia (0.5% isoflurane in O_2) to evoke calcium responses. The standard deviation images of the time-lapse stacks showed greater intensity differences across time frames after aberration correction (**Fig. 5p**, zoomed-in views on the white boxes in **Fig. 5l**), indicative of larger calcium transient magnitude. Indeed, for five example ROIs (1-5, **Fig. 5p**), calcium transients were more apparent and have larger magnitudes in both trial-averaged fluorescence (F) and $\Delta F/F_0$ traces with AO (left and middle panels, **Fig. 5q**), leading to higher orientation selectivity indices for these structures (right panels, **Fig. 5q**).

Over the population of 125 orientation-selective ROIs out of 255 somatic and neuronal structures within the whole FOV, we found statistically significant differences between No AO and AO conditions for both basal fluorescence F_0 (two-sided paired t-test, $p < 0.001$, **Fig. 5r**) and $\Delta F/F_0$ ($p < 0.05$, **Fig. 5s**). Here the increase in basal fluorescence was less than what we observed for glutamate imaging of dendritic spines, because aberration decreases signal brightness of smaller structures such as dendritic spines more than larger structures such as somata[28,33,34]. Similar to glutamate imaging, AO increased the OSIs of neuronal structures (two-sided paired t-test, $p < 0.001$, **Fig. 5t**; for cumulative distributions of OSI, Kolmogorov-Smirnov test, $p < 0.001$, **Fig. 5u**).

Discussion

In this work, we propose NeAT, a general-purpose AO framework for aberration measurement and correction for 2P microscopy using neural fields. Neural fields refer to implicit functions represented by a coordinate-based neural network across spatial coordinates[14]. They have been used for various computational imaging applications[16,27,35–39], including Neural Radiance Fields (NeRF)[13] for 3D scene representation. NeAT has several distinct features that set it apart from NeRF and other neural field applications, as detailed in **Table S1**, which include its incorporation of a physics-based prior specific to the 2P imaging system, its estimation and correction of sample motion and microscopy conjugation errors, and its joint recovery of 3D structural information alongside aberration estimation.

Using the physics-based prior of the 2P imaging system, implemented through an image-formation model that accounts for both aberrations and sample motion, NeAT accurately estimates optical aberrations from a 2P fluorescence image stack without the need for external supervision, even in the presence of motion artifacts during live animal imaging. Importantly, this functionality eliminates the need for integration of AO capabilities into microscope control software, making it applicable to existing custom-built and commercial 2P microscopy systems in general.

Furthermore, NeAT can estimate and correct conjugation errors. Such errors are common in custom-built and commercial microscopes used in general biology laboratories and cause the distortion of the applied corrective phase pattern at the objective lens back focal plane, leading to deteriorated AO performance. NeAT measures the impact of the conjugation errors on calibration aberrations and compensates for them by preemptively transforming the corrective phase pattern before it is displayed on the wavefront-shaping device. This feature would greatly facilitate the broader adoption of AO in a wide range of microscope environments.

Additionally, NeAT simultaneously recovers 3D structural information while estimating aberration during its learning process. For applications where only structural information is needed, this unique capability eliminates the requirement of wavefront-shaping devices or the need for additional imaging with AO correction, greatly lowering system complexity and cost.

We rigorously evaluated NeAT's robustness under various conditions, such as different SNR levels, aberration severity, and motion artifacts. We established the framework's performance limits for accurate and reliable operation, providing valuable guidelines on imaging settings when applying NeAT.

Finally, we applied NeAT to *in vivo* structural and functional imaging of the mouse brain by a commercial microscope, demonstrating its capability in improving image quality for demanding real-life biological applications. NeAT effectively estimates and corrects aberrations deep into the mouse brain, enabling morphological imaging of synapses at 500 μm with improved resolution and contrast. It also improves the signal and accuracy of glutamate and calcium imaging of synapses and neurons in the mouse visual cortex responding to visual stimuli. NeAT's simple implementation, robust performance, and ability to correct for motion and conjugation errors in imaging systems, offer great potential for broader adoption and impact in biological research.

Methods

Custom-built two-photon microscopy with direct wavefront sensing AO

The custom-built two-photon fluorescence microscopy was equipped with a wavefront sensor for DWS and was described previously[40,41] (**Fig. S2a**). A Ti-Sapphire laser (Chameleon Ultra II, Coherent Inc.) was tuned to 920 nm output and was scanned by a pair of carefully conjugated galvos (H2105, Cambridge). Pairs of achromatic doublet lenses (L3-L8) were used to conjugate the surfaces of galvos with a DM (PTT489, Iris AO) and the BFP of an objective lens (CFI Apo LWD ×25, 1.1 NA, 2.0 mm WD, Nikon). During imaging, two-photon excited fluorescence was collected by the same objective, reflected by a dichroic mirror (D2, Di02-R785-25x36, Semrock), and detected by a GaAsP photomultiplier tube (H7422-40, Hamamatsu). For wavefront sensing, the emitted two-photon fluorescence was descanned by the galvo pair, reflected by a dichroic mirror (D1, Di02-R785-25x36, Semrock), and directed to a Shack-Hartmann (SH) sensor through a pair of achromatic lenses (FL = 60, 175 mm). The SH sensor consisted of a lenslet array (Advanced Microoptic Systems GmbH) conjugated to the objective BFP and a CMOS camera (Orca Flash 4.0, Hamamatsu) positioned at the focal plane of the lenslet array.

Commercial two-photon fluorescence microscopy with an AO module

The commercially available multiphoton microscope (Bergamo II, Thorlabs) used a Ti-Sapphire laser (Chameleon Ultra II, Coherent Inc.) tuned to 920 nm or 1000nm for two-photon excitation. An AO module consisted of a liquid crystal SLM (1024 × 1024, HSP1K, Meadowlark Inc.) and two pairs of relay lenses (L1-L4, FL = 200, 50, 500, and 500mm) was added to the beam path between the laser and the microscope. The laser output had its polarization rotated by an achromatic half-wave plate (AHWP05M-980, Thorlabs) to align with the SLM polarization requirement and was expanded 15 times using two beam expanders (GBE03-B, GBE05-B, Thorlabs) to fill the active area of the SLM. The two pairs of relay lenses demagnified the laser output and conjugated the SLM surface to the non-resonant galvo surface within the galvo-resonant-galvo scanning head of the microscope. A pair of scan lenses within the Bergamo II microscope (L5-L6, FL=50 and 200mm) relayed the laser to the BFP of a water-dipping objective (25×, 1.05 NA, 2mm WD, Olympus). Fluorescence emission was collected through the objective

and detected by two GaAsP photomultiplier tubes (PMT 2100, Thorlabs) for two-color imaging of green (525/50 nm emission filter) and red (607/70 nm emission filter) fluorescence, respectively.

Animals and surgical procedures

All animal experiments were conducted in accordance with the National Institutes of Health guidelines for animal research. Procedures and protocols involving mice were approved by the Institutional Animal Care and Use Committee at the University of California, Berkeley. *In vivo* imaging experiments were performed using 2-4-month-old wild-type (C57BL/6J) or Thy1-GFP line M mouse lines.

Cranial window and virus injection surgeries were conducted under anesthesia (2% isoflurane in O_2) following established procedures[31,42]. For *in vivo* glutamate imaging, sparse expression of iGluSnFR3 was achieved in V1 L2/3 by injecting a 1:1 mixture of diluted AAV2/1-Syn-Cre virus (original titer 1.8×10^{13} GC/ml, diluted 10,000-fold in phosphate-buffered saline) and AAV-hSyn-FLEX-iGluSnFR3-v857-SGZ at multiple sites 150-250 µm below pia. 25 nl of the virus mixture was injected at each site. For *in vivo* calcium imaging, dense expression of GCaMP6s and sparse expression of TdTomato was achieved in V1 L2/3 by co-injecting a 1:1:1 mixture of diluted AAV2/1-Syn-Cre virus (original titer 1.8×10^{13} GC/ml, diluted 1,000-fold in phosphate-buffered saline), AAV2/1-CAG-FLEX-tdTomato (6×10^{13} GC/ml), and AAV1-Syn-GCaMP6s-WPRE-SV40 (1×10^{13} GC/ml) at multiple sites 150-250 µm below the pia. 25 nl of the virus mixture was injected at each site. A cranial window, made of a glass coverslip (Fisher Scientific, no. 1.5), was embedded in the craniotomy and sealed in place with Vetbond tissue adhesive (3M). A metal head post was attached to the skull using cyanoacrylate glue and dental acrylic. After 3 weeks of expression and 3 days of habituation for head fixation, *in vivo* imaging was conducted in head-fixed mice under anesthesia (1% isoflurane in O_2) for structural imaging and in lightly anesthetized mice (0.5% isoflurane in O_2) for functional imaging.

Loss function and regularization in self-supervised learning process

The fidelity term $\mathcal{L}(Ag, \hat{g})$ in the loss function (**Eq. 3**) is represented as a convex combination of SSIM[19] and rMSE[20–22] as follows,

$$\mathcal{L}(Ag, \hat{g}) = \gamma\ \mathrm{SSIM}(Ag, \hat{g}) + (1 - \gamma)\ \mathrm{rMSE}(Ag, \hat{g}), \tag{9}$$

where rMSE is defined as

$$\mathrm{rMSE}(Ag, \hat{g}) = \left(\frac{Ag - \hat{g}}{\mathrm{sg}(\hat{g}) + \varepsilon_l}\right)^2. \tag{10}$$

Here $\mathrm{sg}(\cdot)$ denotes a stop-gradient operation that treats its argument as a constant, employed for numerical stability during backpropagation[20]. The parameter γ controls the weight between the two terms. It is set to 0.25 if the RMS contrast of the image stack's background pixels, *i.e.*, $\varepsilon_l = \sigma_b(g_{bfr})$, is larger than 0.03, where $\sigma_b(\cdot)$ computes the standard deviation of the background pixels of the operand. If the contrast is smaller than 0.02, γ is set to 1.0. Otherwise, γ is linearly interpolated between 0.25 and 1.0. Here, g_{bfr} represents a background-fluctuation-removed version of g, introduced to remove any unwanted low-frequency fluctuations in the images that could otherwise exaggerate the standard deviation.

The regularization term $\mathcal{R}(s)$ in the loss function (**Eq. 3**) are designed to render spatially sparse and smooth structural details, serving as a generic prior that reflects structural features of mouse brain neurons. It includes three regularization terms: second-order total variation (TV) $\mathcal{R}_{tv}(s)$[23,24], L1 regularization $\mathcal{R}_{\mathrm{L1}}(s)$, and nonlinear diffusion (NLD) $\mathcal{R}_{\mathrm{NLD}}(s)$[25].

First, second-order TV $\mathcal{R}_{tv}(s)$ aims to recover smooth profiles from noisy measurements by sparsifying the spatial gradient components. Unlike first-order TV[43], which uses first-order derivatives, second-order TV uses second-order derivatives to avoid staircase artifacts[23,24]. In our implementation, we further applied a nonlinear tone mapping function[20], an approximated logarithmic function (**Eq. 12**), which strongly penalizes errors in regions with low intensity values. For simplicity, the spatial coordinates (x, y, z) are expressed as (x_1, x_2, x_3) below.

$$tv(s) = \sum_{1 \le i \le j \le 3} \left| \frac{\partial^2 s}{\partial x_i \, \partial x_j} \right|, \tag{11}$$

$$\mathcal{R}_{tv}(s) = \log(tv(s) + \varepsilon_{tv}) \simeq \frac{tv(s)}{\mathrm{sg}(tv) + \varepsilon_{tv}}, \tag{12}$$

where $\mathrm{sg}(\cdot)$ indicates the same stop-gradient operation as above, and ε_{tv} is determined from the input image stack g as the smallest standard deviation of second-order difference $tv(g)$, that is,

$$\varepsilon_{tv} = \min\left(\sigma_b\left(\left|\frac{\partial^2 g}{\partial x_i \, \partial x_j}\right|\right)\right), \qquad 1 \le i \le j \le 3. \tag{13}$$

Second, L1 regularization $\mathcal{R}_{\mathrm{L1}}(s)$ helps to render the structure s with spatially sparse features by adding a penalty based on the absolute value of s as follows,

$$\mathcal{R}_{\mathrm{L1}}(s) = \log(|s| + \varepsilon_{L1}) \simeq \frac{|s|}{\mathrm{sg}(|s|) + \varepsilon_{L1}}. \tag{14}$$

Here $\varepsilon_{L1} = \sigma_b(|g_{bfr}|)$ and the same logarithmic tone mapping function[20] (**Eq. 12**) is applied on the top of the absolute value.

Lastly, NLD regularization[25] $\mathcal{R}_{\mathrm{NLD}}(s)$ constrains the magnitude of the first-order difference of the structure s, computed along the depth axis z. This suppresses slowly varying spatial components while preventing the structure from fitting to rapidly varying axial features that sparsity-promoting regularizations might favor. This regularization balances the influence of the first two terms, allowing the structure to retain desirable details. It is written as

$$\mathcal{R}_{\mathrm{NLD}}(s) = \left|\frac{\partial s}{\partial z}\right|\Bigg|_{\delta,[a,b]}, \tag{15}$$

where $f|_{\delta,[a,b]} \equiv \max(f, b) + \delta \max(a, \min(f, b)) + \min(f, a)$. For all results presented in this manuscript, $\delta = 0.1, a = 0.005, b = 2.0$.

Together, the summation of the regularization terms is expressed as

$$\mathcal{R}(s) = \lambda_{tv}\mathcal{R}_{tv}(s) + \lambda_{\mathrm{L1}}\mathcal{R}_{\mathrm{L1}}(s) + \lambda_{\mathrm{NLD}}\mathcal{R}_{\mathrm{NLD}}(s), \tag{16}$$

where $\lambda_{tv} = 0.005, \lambda_{\mathrm{L1}} = 0.01, \lambda_{\mathrm{NLD}} = 10^{-6}$.

Baseline term in image formation

The baseline term b is modeled as low rank to account for the offset due to baseline fluorescence or noise and potential power decrease along the depth axis caused by scattering in deep tissue imaging. b is represented as the sum of rank-1 tensors, with rank R less than the number of pixels along x, y, and z-axes, N_x, N_y, N_z, and set to $R = 5$ here:

$$b = \sum_{r=1}^{R} b_{z,r} \times b_{y,r} \times b_{x,r}, \tag{17}$$

where $b_{x,r}, b_{y,r}, b_{z,r}$ are learnable 2D tensors to represent baseline components along the $x, y,$ and z axes, respectively. These tensors are initialized with the value $\left(0.1\,\sigma_b(|g_{bfr}|)\right)^{1/3}$. By limiting the rank of the baseline model, we constrain it to capture only low-spatial-frequency baseline features, thereby effectively separating the baseline from the sample features.

Two-step learning process

The weights of the neural network θ representing structure s, Zernike coefficients α (thus PSF $h(\boldsymbol{r};\alpha)$), and baseline term b in the image-formation model are optimized in a two-step learning process[27]. The first step only adjusts neural network weights for s, while the Zernike coefficients α and baseline b remain fixed after initialization. It conditions the randomly initialized neural network, using the loss function:

$$\theta^* = \underset{\theta}{\operatorname{argmin}} \left(\operatorname{SSIM}\left(c g_{lp}, f_\theta(\boldsymbol{r})\right)\right), \qquad c \geq 1 \tag{18}$$

where g_{lp} is a low pass filtered image stack with an isotropic Gaussian filter. Optimization is performed using the RAdam optimizer[44] with an initial learning rate of 10^{-2}, $\beta_1 = 0.9$, and $\beta_2 = 0.999$ for 5000 epochs. The learning rate schedule follows an exponential decay down to 10^{-3} by the end of the epoch.

The second step updates neural network weights θ, Zernike coefficients α, and baseline b using the loss function (**Eq. 3**). For this learning process, the initial learning rate is set to 4×10^{-3} with the same RAdam optimizer, keeping β_1 and β_2 unchanged, running for 5000 epochs. The learning rate schedule again follows an exponential decay, this time down to 10^{-6} by the end of the epoch.

All computational implementations are performed on a machine equipped with an NVIDIA RTX 4090 GPU, an Intel i9-13900K CPU, and 80 GB of RAM. The estimation times for the results in the main figures are detailed in **Table S2**, along with their corresponding experimental settings.

Preprocessing of 3D image stacks from *in vivo* experiments

In our experimental settings, the raw 3D experimental fluorescence image stacks have dimensions of $N_f \times N_z \times N_y \times N_x$, where N_f denotes the number of frames per z-axis slice, N_z the number of z-axis slices, and N_x and N_y the number of pixels along the x- and y-axes, respectively. Here N_f frames are acquired per z-axis slice to reduce the effect of Gaussian noise through averaging. In *in vivo* imaging experiments, the frames acquired at the same z need to be registered before averaging to correct for the artifacts between frames. We used a customized ImageJ plugin to register the frames for each z-axis slice and average the registered frames to obtain the image stack with dimensions of $N_z \times N_y \times N_x$. This plugin is available in our public repository.

Motion correction of image stacks by NeAT

Image stacks acquired *in vivo* can contain motion artifacts caused by heartbeats or body movements. Although preprocessing removes the motion artifacts for frames acquired at the same *z* depth as described above, motion between frames at different *z* depths also needs to be corrected. Failing to so would lead to errors in aberration estimation and structural recovery (**Fig. S3**). NeAT incorporates motion correction across *z* slices into its learning process and outperform existing algorithms such as StackReg in ImageJ (**Fig. S8**).

NeAT assigns an affine transformation matrix, A_{n_z} $(n_z = 1,2,\cdots,N_z)$, to each *z* slice to correct translation, rotation, scaling, and shear caused by the sample's motion. It corrects motion by updating these matrices throughout the learning process. The matrices are initialized as identity matrices. We used the RAdam optimizer[44] for the motion correction process, with an initial learning rate of 0.1, $\beta_1 = 0.9$, and $\beta_2 = 0.999$. More details are available in our public repository.

Calculation of signal-to-noise ratio

We assumed a linear relationship between grayscale value (p) and photon count per pixel (c), with $p = \beta c$. Since the photon count per pixel theoretically follows a Poissionian distribution, β can be computed as the ratio of the variance of p to its mean. For the cutoff SNR analysis, we calculated β for the PMT in the custom-build microscope under different control voltages, observing gains of 7.83 at a control voltage of 0.7 V (used for acquiring images from 1-μm fluorescence beads, **Figs. 2j-l**) and 21.8 at a control voltage of 0.8 V (used for fixed Thy1-GFP mouse brain slice imaging, **Figs. 2m-o**).

Next, we classified the pixels in an image stack as either signal or background pixels using a classification method described previously[27]. We then calculated the SNR of the image stack as

$$\mathrm{SNR} = \frac{\bar{y}/\beta}{\sqrt{\bar{y}/\beta}} = \sqrt{\bar{y}/\beta}, \tag{19}$$

where $\bar{y}$ is the mean of the signal pixels.

In vivo imaging of visually evoked glutamate and calcium activity

Visual stimuli were generated in MATLAB using the Psychophysics Toolbox[45,46]and presented 15 cm from the left eye of the mouse on a gamma-corrected, LED-backlit LCD monitor with a mean luminance of 20 cd·m^{-2}. We divided the monitor into a 3 × 3 grid and presented 1-s-long uniform flashes in a pseudorandom sequence in one of the 9 grids, while recording fluorescence images with a 2 mm by 2 mm FOV. Analyzing these images allowed us to identify the cortical region that responded to the center of the monitor. We then imaged this cortical region at smaller pixel sizes to measure glutamate and calcium activity of synapses and neurons towards oriented drifting grating stimulation in mice under light anesthesia (0.5% isoflurane in O_2). Full-field gratings of 100% contrast, a spatial frequency of 0.04 cycles per degree, and a temporal frequency of 2 Hz drifting in eight directions (0° to 315° at 45° increments) were presented in pseudorandom sequences. For glutamate imaging (*x* and *y* pixel size: 0.125 μm/pixel), each grating stimulus lasted 2 s with a 1-s presentation of a gray screen before and after the stimulus. For calcium imaging (*x* and *y* pixel size: 0.945 μm/pixel), each grating stimulus lasted 2 s with a 1-s gray screen presentation before and a 3-s gray screen presentation after the stimulus. Each stimulus was repeated for 10 trials per imaging session.

Functional image analysis

Images were processed with custom Python code. Glutamate time-lapse images were registered using iterative phase correlation with polar transform, and calcium time-lapse images were registered with the StackReg package[47]. Regions of interest (ROIs) were manually drawn in ImageJ using the circular selection tool on the mean intensity projection of the glutamate time-lapse images and elliptical selection tool for the GCaMP6s time-lapse images. The ROIs were then imported into a Python environment to extract pixel values within the ROIs, which were averaged to obtain the raw fluorescence signal F for each ROI.

The glutamate transient $\Delta F/F_0$ was calculated as $(F - F_0)/F_0$, where F_0 represents the basal fluorescence, defined as the average fluorescence signal during the 1-s pre-stimulus gray-screen presentation period, excluding the highest 5% of values in F from the calculation.

For calcium images, due to higher labeling density, we removed neuropil contamination. We calculated F_{neuropil} as the averaged fluorescence signal from the neuropil area[32] (defined as the pixels that were 2 to 20 pixels off the ROI border) and computed $\Delta F_{\text{neuropil}}$ as $F_{\text{neuropil}} - F_{0,\text{ neuropil}}$, where $F_{0,\text{ neuropil}}$ is the mean of F_{neuropil} during the 1-s pre-stimulus period. Then,

$\Delta F_{\text{neuropil}}$ was multiplied by 0.7 and subtracted from F to obtain F_{true}. $\Delta F/F_0$ was then computed as $(F_{\text{true}} - F_{0,\text{true}})/F_{0,\text{true}}$, with $F_{0,\text{true}}$ defined as the mean of F_{true} during the 1-s pre-stimulus period.

Trial-averaged $\Delta F/F_0$ was calculated as the average of 10 trials. Peak $\Delta F/F_0$ was defined as the maximal trial-averaged $\Delta F/F_0$ within the 2-s drifting grating presentation. Response R for each drifting grating direction was defined as the averaged $\Delta F/F_0$ across the 2-s drifting-grating stimulus presentation, with negative responses set to zero.

For glutamate images, an ROI was considered responsive to visual stimulation if its peak $\Delta F/F_0$ was greater than 3 times the standard deviation of the trial-averaged $\Delta F/F_0$ within the 2-s stimulus period[48,49] and if the peak $\Delta F/F_0$ was above 5%[50]. For calcium images, an ROI was considered active if its maximal $\Delta F/F_0$ was above 10%[42,51] and visually responsive if its activity during at least one visual stimulus type was significantly higher than its activity during the pre-stimulus period, as determined by one-way ANOVA with $p < 0.01$.

Orientation selectivity analysis

For each ROI, its tuning curve $R_{fit}(\theta)$ was defined as the fitted curve to $R(\theta)$ with a bimodal Gaussian function[30]:

$$R_{fit}(\theta) = R_0 + A_1\, e^{-\frac{ang(\theta-\theta_{pref})^2}{2\sigma^2}} + A_2\, e^{-\frac{ang(\theta-\theta_{pref}+180°)^2}{2\sigma^2}}, \tag{20}$$

where $ang(x) = \min(|x|, |x - 360°|, |x + 360°|)$, which wraps the angular values onto the interval between 0° and 180°. Responses to the different drifting direction $R(\theta)$ were fitted to the model to minimize the mean square error between the model and responses, with R_0, A_1, A_2 constrained to non-negative values, and σ constrained to be larger than 22.5°[52], given that the angle step was 45°.

ROIs were considered orientation-sensitive (OS) if their responses across 8 different drifting grating stimuli were significantly different by one-way ANOVA ($p < 0.05$)[31,50] and if their responses were well-fit to the bimodal Gaussian model[51]. The goodness of the fit was assessed by calculating the error E and the coefficient of determination $\Re^2$:

$$E = \sum_{n=0}^{7} \left(R(\theta) - R_{fit}(\theta)\right)^2\Big|_{\theta=(45n)°}, \qquad \Re^2 = 1 - \frac{E}{\sum_{n=0}^{7}(R(\theta) - \bar{R})^2|_{\theta=(45n)°}}, \tag{21}$$

where $\bar{R}$ is the mean of $R(\theta)$. The criteria for a good fit were $E < 0.01$ and $\Re^2 > 0.5$. The fitted response was used to calculate orientation sensitivity index (OSI) as $\frac{R_{\text{pref}} - R_{\text{ortho}}}{R_{\text{pref}} + R_{\text{ortho}}}$, where R_{pref} and R_{ortho} are the responses at θ_{pref} and $\theta_{\text{ortho}}(= \theta_{\text{pref}} + 90^\circ)$, respectively.

Statistics

Standard functions from the Scipy package in Python were used to perform statistical tests, including two-sided paired t-test, one-way ANOVA, and Kolmogorov-Smirnov test. Statistical significance was defined as $*p < 0.05$, $***p < 0.01$, and $***p < 0.001$.

Data availability

This section will be completed once the public repository is created following the peer review and patent publication.

Code availability

This section will be completed once the public repository is created following the peer review and patent publication.

Acknowledgements

This work was supported by the Weill Neurohub, National Institutes of Health (U01NS118300), and Department of Energy (DE-SC0021986).

Author contribution

I.K. and N.J. conceived the project. N.J. supervised the project. I.K., H.K. designed and performed experiments. R.N. prepared samples. I.K. developed the algorithm with input from S.X.Y. and N.J. All authors participated in writing the paper.

Competing interests

I.K. and N.J. are listed as inventors on a patent related to the technology described in this study (U.S. patent application No. 63/707.628). No other authors declare competing interests.

Ethics

All animal experiments were conducted according to the National Institutes of Health guidelines for animal research. Procedures and protocols on mice were approved by the Institutional Animal Care and Use Committee at the University of California, Berkeley (AUP-2020-06-13343).

References

1. Xu, C., Nedergaard, M., Fowell, D. J., Friedl, P. & Ji, N. Multiphoton fluorescence microscopy for in vivo imaging. *Cell* **187**, 4458–4487 (2024).
2. Ji, N. Adaptive optical fluorescence microscopy. *Nat Methods* **14**, 374–380 (2017).
3. Hampson, K. M. *et al.* Adaptive optics for high-resolution imaging. *Nature Reviews Methods Primers* **1**, 68 (2021).
4. Zhang, Q. *et al.* Adaptive optics for optical microscopy [Invited]. *Biomed. Opt. Express* **14**, 1732 (2023).
5. Booth, M. J. Adaptive optical microscopy: the ongoing quest for a perfect image. *Light Sci Appl* **3**, e165–e165 (2014).
6. Rodríguez, C. & Ji, N. Adaptive optical microscopy for neurobiology. *Current opinion in neurobiology* **50**, 83–91 (2018).
7. Paine, S. W. & Fienup, J. R. Machine learning for improved image-based wavefront sensing. *Opt. Lett.* **43**, 1235 (2018).
8. Saha, D. *et al.* Practical sensorless aberration estimation for 3D microscopy with deep learning. *Opt. Express* **28**, 29044 (2020).
9. Hu, Q. *et al.* Universal adaptive optics for microscopy through embedded neural network control. *Light: Science & Applications* **12**, 270 (2023).
10. Allan, G., Kang, I., Douglas, E. S., Barbastathis, G. & Cahoy, K. Deep residual learning for low-order wavefront sensing in high-contrast imaging systems. *Opt. Express* **28**, 26267 (2020).
11. Feng, B. Y. *et al.* NeuWS: Neural wavefront shaping for guidestar-free imaging through static and dynamic scattering media. *Science Advances* **9**, eadg4671 (2023).

12. Bostan, E., Heckel, R., Chen, M., Kellman, M. & Waller, L. Deep phase decoder: self-calibrating phase microscopy with an untrained deep neural network. *Optica* **7**, 559 (2020).
13. Mildenhall, B. *et al.* NeRF: representing scenes as neural radiance fields for view synthesis. *Commun. ACM* **65**, 99–106 (2022).
14. Xie, Y. *et al.* Neural fields in visual computing and beyond. in *Computer Graphics Forum* vol. 41 641–676 (Wiley Online Library, 2022).
15. Goodman, J. W. *Introduction to Fourier Optics*. (Roberts and Company publishers, 2005).
16. Liu, R., Sun, Y., Zhu, J., Tian, L. & Kamilov, U. S. Recovery of continuous 3d refractive index maps from discrete intensity-only measurements using neural fields. *Nature Machine Intelligence* **4**, 781–791 (2022).
17. Tancik, M. *et al.* Fourier Features Let Networks Learn High Frequency Functions in Low Dimensional Domains. in *Advances in Neural Information Processing Systems* (eds. Larochelle, H., Ranzato, M., Hadsell, R., Balcan, M. F. & Lin, H.) vol. 33 7537–7547 (Curran Associates, Inc., 2020).
18. Hornik, K., Stinchcombe, M. & White, H. Multilayer feedforward networks are universal approximators. *Neural Networks* **2**, 359–366 (1989).
19. Wang, Z., Bovik, A. C., Sheikh, H. R. & Simoncelli, E. P. Image quality assessment: from error visibility to structural similarity. *IEEE transactions on image processing* **13**, 600–612 (2004).
20. Mildenhall, B., Hedman, P., Martin-Brualla, R., Srinivasan, P. P. & Barron, J. T. Nerf in the dark: High dynamic range view synthesis from noisy raw images. in *Proceedings of the IEEE/CVF conference on computer vision and pattern recognition* 16190–16199 (2022).

21. Lehtinen, J. *et al.* Noise2Noise: Learning Image Restoration without Clean Data. in *Proceedings of the 35th International Conference on Machine Learning* (eds. Dy, J. & Krause, A.) vol. 80 2965–2974 (PMLR, 2018).
22. Rousselle, F., Knaus, C. & Zwicker, M. Adaptive sampling and reconstruction using greedy error minimization. *ACM Transactions on Graphics (TOG)* **30**, 1–12 (2011).
23. Chan, T., Marquina, A. & Mulet, P. High-order total variation-based image restoration. *SIAM Journal on Scientific Computing* **22**, 503–516 (2000).
24. Knoll, F., Bredies, K., Pock, T. & Stollberger, R. Second order total generalized variation (TGV) for MRI. *Magnetic resonance in medicine* **65**, 480–491 (2011).
25. Tian, L., Petruccelli, J. C. & Barbastathis, G. Nonlinear diffusion regularization for transport of intensity phase imaging. *Optics letters* **37**, 4131–4133 (2012).
26. Turcotte, R., Liang, Y. & Ji, N. Adaptive optical versus spherical aberration corrections for in vivo brain imaging. *Biomed. Opt. Express* **8**, 3891–3902 (2017).
27. Kang, I., Zhang, Q., Yu, S. X. & Ji, N. Coordinate-based neural representations for computational adaptive optics in widefield microscopy. *Nature Machine Intelligence* **6**, 714–725 (2024).
28. Ji, N., Sato, T. R. & Betzig, E. Characterization and adaptive optical correction of aberrations during in vivo imaging in the mouse cortex. *Proc. Natl. Acad. Sci. U.S.A.* **109**, 22–27 (2012).
29. Aggarwal, A. *et al.* Glutamate indicators with improved activation kinetics and localization for imaging synaptic transmission. *Nature methods* **20**, 925–934 (2023).
30. Carandini, M. & Ferster, D. Membrane potential and firing rate in cat primary visual cortex. *Journal of Neuroscience* **20**, 470–484 (2000).

31. Chen, W. *et al.* High-throughput volumetric mapping of synaptic transmission. *Nature Methods* 1–8 (2024).

32. Chen, T.-W. *et al.* Ultrasensitive fluorescent proteins for imaging neuronal activity. *Nature* **499**, 295–300 (2013).

33. Wang, C. *et al.* Multiplexed aberration measurement for deep tissue imaging in vivo. *Nat Methods* **11**, 1037–1040 (2014).

34. Rodríguez, C. *et al.* An adaptive optics module for deep tissue multiphoton imaging in vivo. *Nature methods* **18**, 1259–1264 (2021).

35. Barron, J. T., Mildenhall, B., Verbin, D., Srinivasan, P. P. & Hedman, P. Mip-nerf 360: Unbounded anti-aliased neural radiance fields. in *Proceedings of the IEEE/CVF conference on computer vision and pattern recognition* 5470–5479 (2022).

36. Zhao, B., Levis, A., Connor, L., Srinivasan, P. P. & Bouman, K. L. Single View Refractive Index Tomography with Neural Fields. in *Proceedings of the IEEE/CVF Conference on Computer Vision and Pattern Recognition (CVPR)* 25358–25367 (2024).

37. He, R., Li, Y., Chen, J. & Xue, Y. Fluorescence Diffraction Tomography using Explicit Neural Fields. *arXiv preprint arXiv:2407.16657* (2024).

38. Cao, R., Liu, F. L., Yeh, L.-H. & Waller, L. Dynamic Structured Illumination Microscopy with a Neural Space-time Model. Preprint at http://arxiv.org/abs/2206.01397 (2022).

39. Shen, S. *et al.* Non-line-of-sight imaging via neural transient fields. *IEEE Transactions on Pattern Analysis and Machine Intelligence* **43**, 2257–2268 (2021).

40. Li, Z. *et al.* Fast widefield imaging of neuronal structure and function with optical sectioning in vivo. *Sci. Adv.* **6**, eaaz3870 (2020).

41. Zhang, Q. *et al.* Retinal microvascular and neuronal pathologies probed in vivo by adaptive optical two-photon fluorescence microscopy. *Elife* **12**, e84853 (2023).

42. Sun, W., Tan, Z., Mensh, B. D. & Ji, N. Thalamus provides layer 4 of primary visual cortex with orientation-and direction-tuned inputs. *Nature neuroscience* **19**, 308–315 (2016).

43. Beck, A. & Teboulle, M. Fast Gradient-Based Algorithms for Constrained Total Variation Image Denoising and Deblurring Problems. *IEEE Trans. on Image Process.* **18**, 2419–2434 (2009).

44. Liu, L. *et al.* On the variance of the adaptive learning rate and beyond. *arXiv preprint arXiv:1908.03265* (2019).

45. Brainard, D. H. & Vision, S. The psychophysics toolbox. *Spatial vision* **10**, 433–436 (1997).

46. Kleiner, M., Brainard, D. & Pelli, D. What's new in Psychtoolbox-3? (2007).

47. Thévenaz, P., Ruttimann, U. E. & Unser, M. A Pyramid Approach to Subpixel Registration Based on Intensity. *IEEE Transactions on Image Processing* **7**, 27–41 (1998).

48. Marvin, J. S. *et al.* Stability, affinity, and chromatic variants of the glutamate sensor iGluSnFR. *Nature methods* **15**, 936–939 (2018).

49. Xie, Y. *et al.* Resolution of high-frequency mesoscale intracortical maps using the genetically encoded glutamate sensor iGluSnFR. *Journal of Neuroscience* **36**, 1261–1272 (2016).

50. Chen, W. *et al.* In vivo volumetric imaging of calcium and glutamate activity at synapses with high spatiotemporal resolution. *Nature communications* **12**, 6630 (2021).

51. Liang, Y., Lu, R., Borges, K. & Ji, N. Stimulus edges induce orientation tuning in superior colliculus. *Nature Communications* **14**, 4756 (2023).

52. Mazurek, M., Kager, M. & Van Hooser, S. D. Robust quantification of orientation selectivity and direction selectivity. *Frontiers in neural circuits* **8**, 92 (2014).

Figures

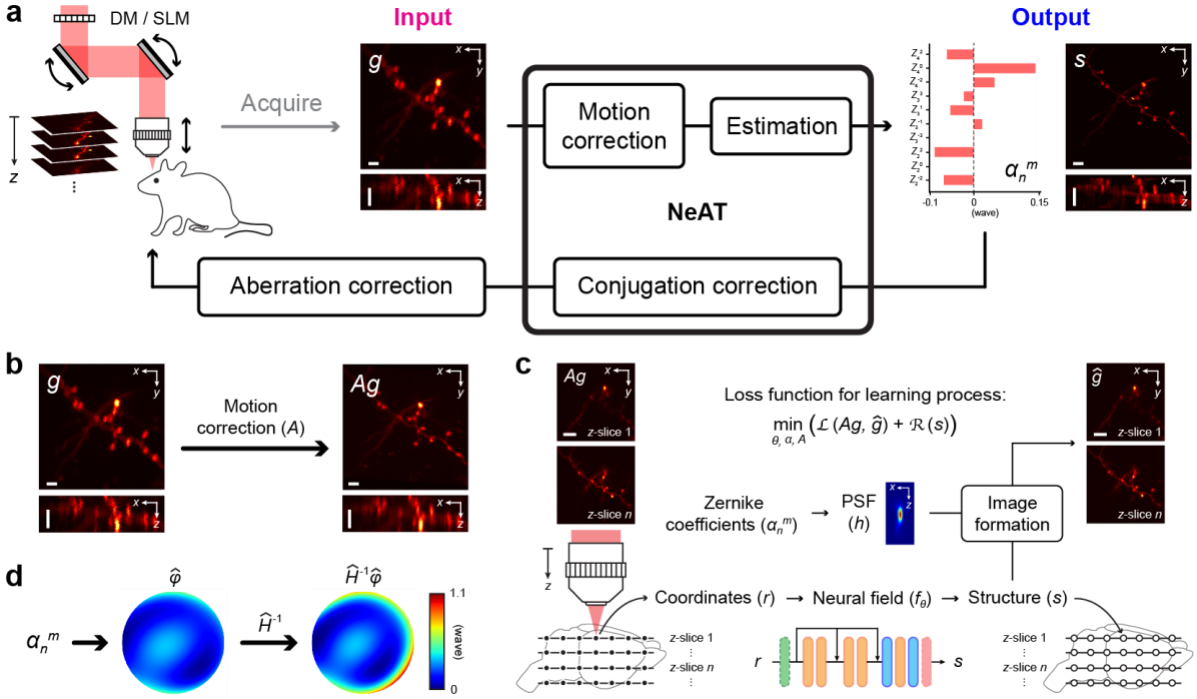

Figure 1. NeAT estimates aberration and recovers structure from a 3D input image stack. (a) Schematic of NeAT's functions and its systematic integration into adaptive optics (AO) imaging pipeline. A 3D two-photon (2P) fluorescence image stack, acquired through *z*-axis scanning, serves as the input, and the 3D structure is the output. Lateral (*xy*) and axial (*xz*) maximum intensity projections (MIPs) of the input image stack and structure are shown. NeAT's capabilities include motion correction, as well as aberration and structural estimation, all of which are performed during the learning process in **c**. If present, NeAT estimates and compensates for conjugation errors within the imaging system. The estimated aberration is then used for correction using deformable mirrors (DM) or spatial light modulators (SLM). Scale bar: 5 µm. **(b)** If present, motion artifacts in g are corrected by applying learnable transformations A. **(c)** The structure is represented as a neural field, while Zernike coefficients define the point spread function (PSF, h). Axial MIP of the PSF is shown. Together, they generate a computationally reproduced image stack, which is updated during the learning process to closely match Ag, achieved by optimizing network weights (θ), Zernike coefficients (α), and motion correction transformations (A). **(d)** Upon completion of the learning process, any conjugation errors in the imaging system, if present, are estimated as $\hat{H}$ and compensated for by applying its inverse to the corrective phase pattern ($\hat{\varphi}$), derived from the learned Zernike coefficients. The fully corrected aberration pattern ($\hat{H}^{-1}\hat{\varphi}$) can then be used for real-time aberration correction and for acquiring an image stack in the subsequent AO iteration. Scale bars: **(a, b)** 5 µm, **(c)** 10 µm.

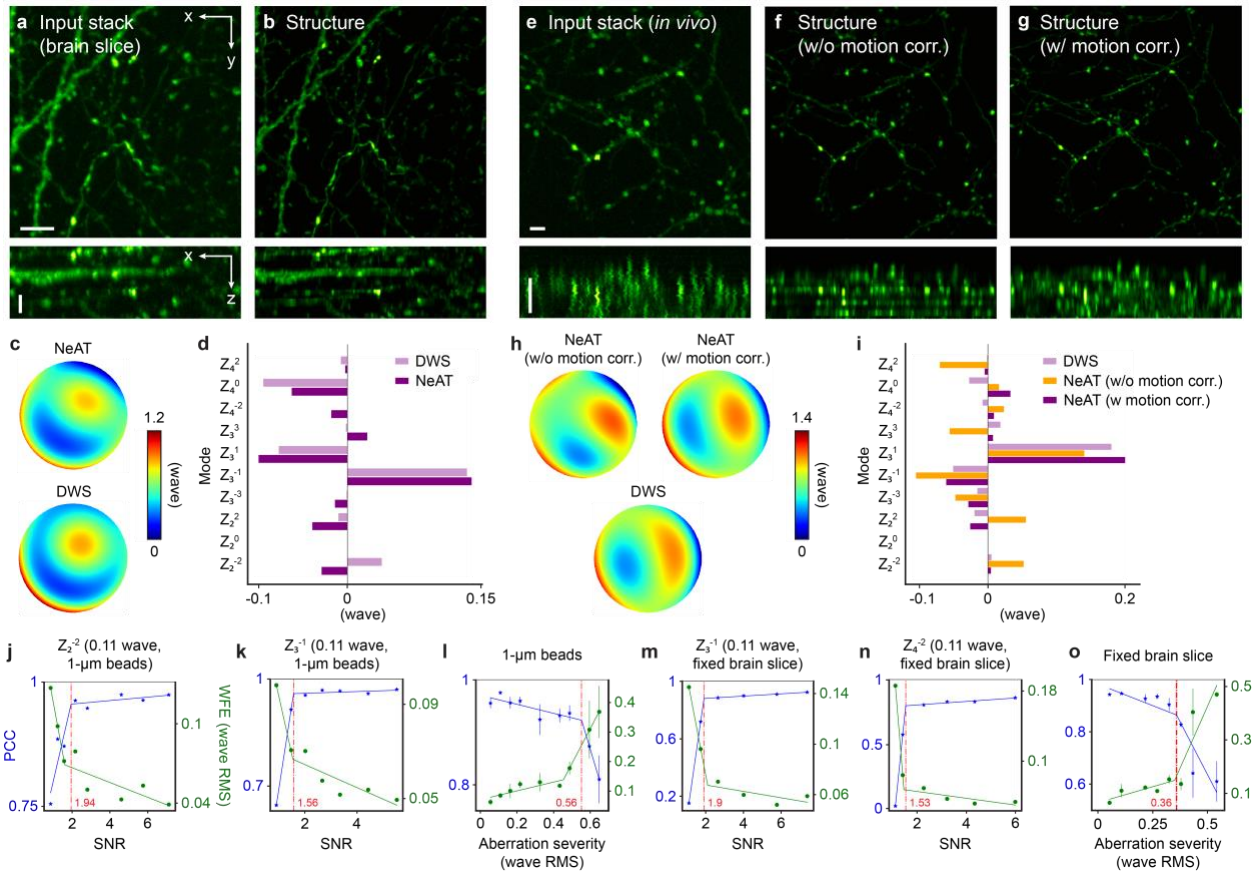

Figure 2. Performance characterization with direct wavefront sensing (DWS) AO in a custom-built 2P microscope. (a) Lateral (*xy*) and axial (*xz*) maximal intensity projections (MIPs) of an input image stack to NeAT from a fixed Thy1-GFP line M mouse brain slice. **(b)** Lateral and axial MIPs of the 3D neuronal structure recovered and **(c)** aberration estimated by NeAT, as well as aberration measured by DWS. **(d)** Zernike coefficients of aberrations in **c**. **(e)** Lateral and axial MIPs of an input image stack acquired *in vivo* from a Thy1-GFP line M mouse brain, with motion artifacts visible in *xz*. **(f,g)** Lateral axial MIPs of the structures recovered by NeAT without **(f)** and with **(g)** motion correction. **(h)** Aberrations estimated by NeAT without and with motion correction, respectively, and measured by DWS. **(i)** Zernike coefficients for aberrations in **h**. **(j,k)** Performance versus SNR using 1-μm-diameter beads under primary astigmatism **(j)** and primary coma **(k)**. PCC: Pearson correlation coefficient between recovered structures; WFE: wavefront error. **(l)** Performance versus aberration severity evaluated using 1-μm-diameter beads. **(m,n)** Performance versus SNR using a fixed mouse brain slice under primary coma **(m)** and secondary astigmatism **(n)**. **(o)** Performance versus aberration severity evaluated using brain slice. Scale bars: 5 μm.

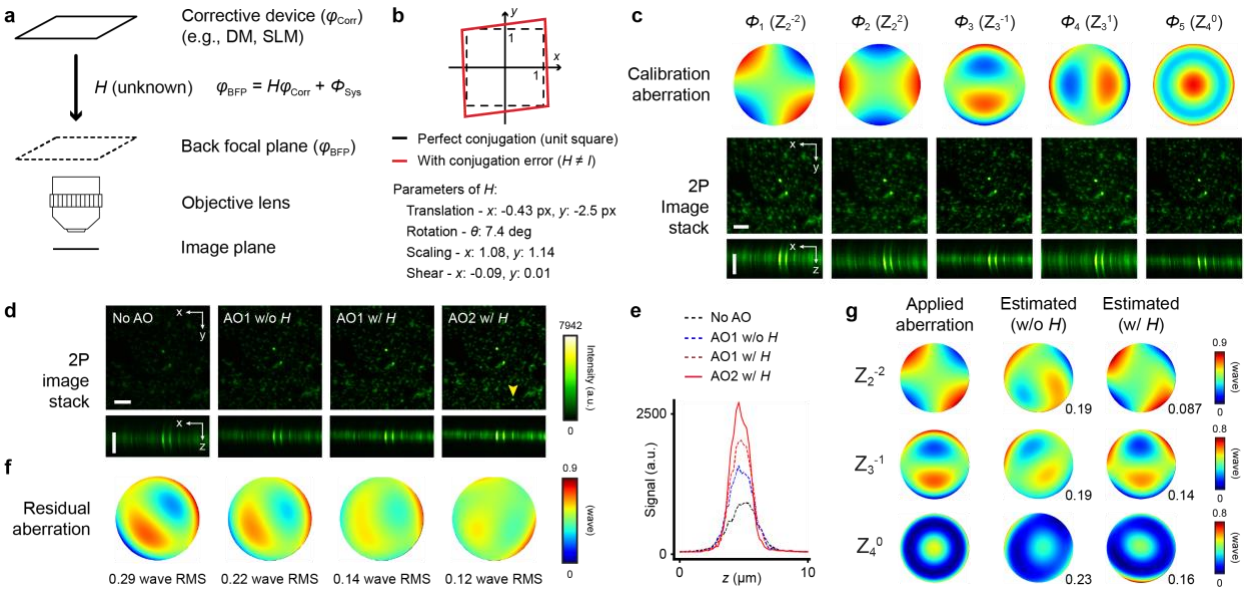

Figure 3. NeAT corrects for conjugation errors in a commercial microscope. (a) Conjugation errors transform corrective pattern φ_{Corr} on SLM to $\varphi_{\mathrm{BFP}} = H\varphi_{Corr} + \Phi_{Sys}$ at objective lens back focal plane. Φ_{Sys}: system aberration. **(b)** H with example affine parameters translates, rotates, scales, and shears a unit square (black dashed square) to a parallelogram (red). **(c)** H is determined from image stacks of 200-nm-diameter beads acquired with a calibration aberration ($\Phi_n, n = 1,2,\cdots,5$) applied to SLM. Lateral (*xy*) and axial (*xz*) MIPs of the calibration image stacks are shown. **(d)** Lateral and axial MIPs of image stacks of 200-nm-diameter beads acquired without system aberration correction ('No AO'), after one iteration of AO without ('AO1 w/o *H*') and with ('AO1 w/*H*') conjugation correction, and after two iterations of AO with conjugation correction ('AO2 w/*H*'). **(e)** Axial signal profiles of the bead marked by yellow arrowhead in **d**. **(f)** Residual aberrations estimated by NeAT from image stacks in **d**. **(g)** Left to right: aberrations (with 0.3 wave RMS) applied to SLM, estimated aberration by NeAT without conjugation correction, and estimated aberration by NeAT with conjugation correction from bead image stacks acquired with the applied aberration. Numbers to the bottom right of estimated aberrations: difference (in wave RMS) between estimated aberration and applied aberration. Scale bars: 5 μm.

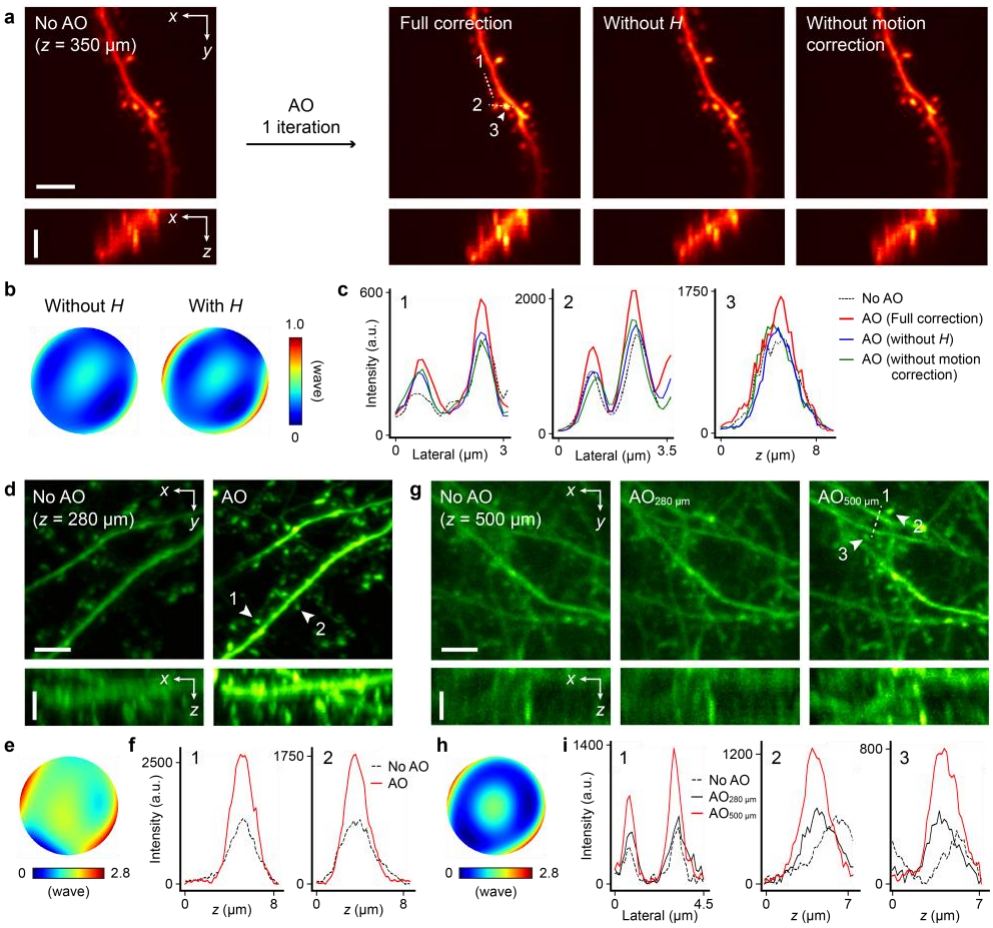

Figure 4. Real-time aberration correction by NeAT for *in vivo* structural imaging. (a) Lateral (*xy*) and axial (*xz*) MIPs of image stacks of tdTomato-expressing dendrite and dendritic spines at 350 μm depth acquired with system aberration correction only ("No AO", used as input to NeAT), with corrective wavefront estimated by NeAT with both conjugation and motion corrections ("Full correction"), with motion correction only ("Without H"), and with conjugation correction only ("Without motion correction"). **(b)** Estimated aberrations by NeAT without and with conjugation correction. **(c)** Lateral signal profiles along dashed lines and axial signal profiles of spine indicated by arrowhead in **a**. **(d)** Lateral and axial MIPs of Thy1-GFP line M mouse dendrites at 280 μm depth acquired without (used as input to NeAT) and with correcting sample-induced aberration by NeAT. **(e)** Estimated aberration by NeAT. **(f)** Axial profiles of dendritic spines marked by arrowheads in **d**. **(g)** Lateral and axial MIPs of neuronal processes at 500 μm depth, acquired with system aberration correction only ("No AO"), aberration correction at 280 μm ("$AO_{280\ \mu m}$", used as input to NeAT; wavefront in **e**), and aberration correction at 500 μm ("$AO_{500\ \mu m}$") **(h)** Sample-induced aberration at 500 μm. **(i)** Lateral profiles along dashed line and axial profiles of spines indicated by arrowheads in **g**. **(a, d, g)** Top: lateral (*xy*) MIPs. Bottom: axial (*xz*) MIPs. Scale bars: 5 μm.

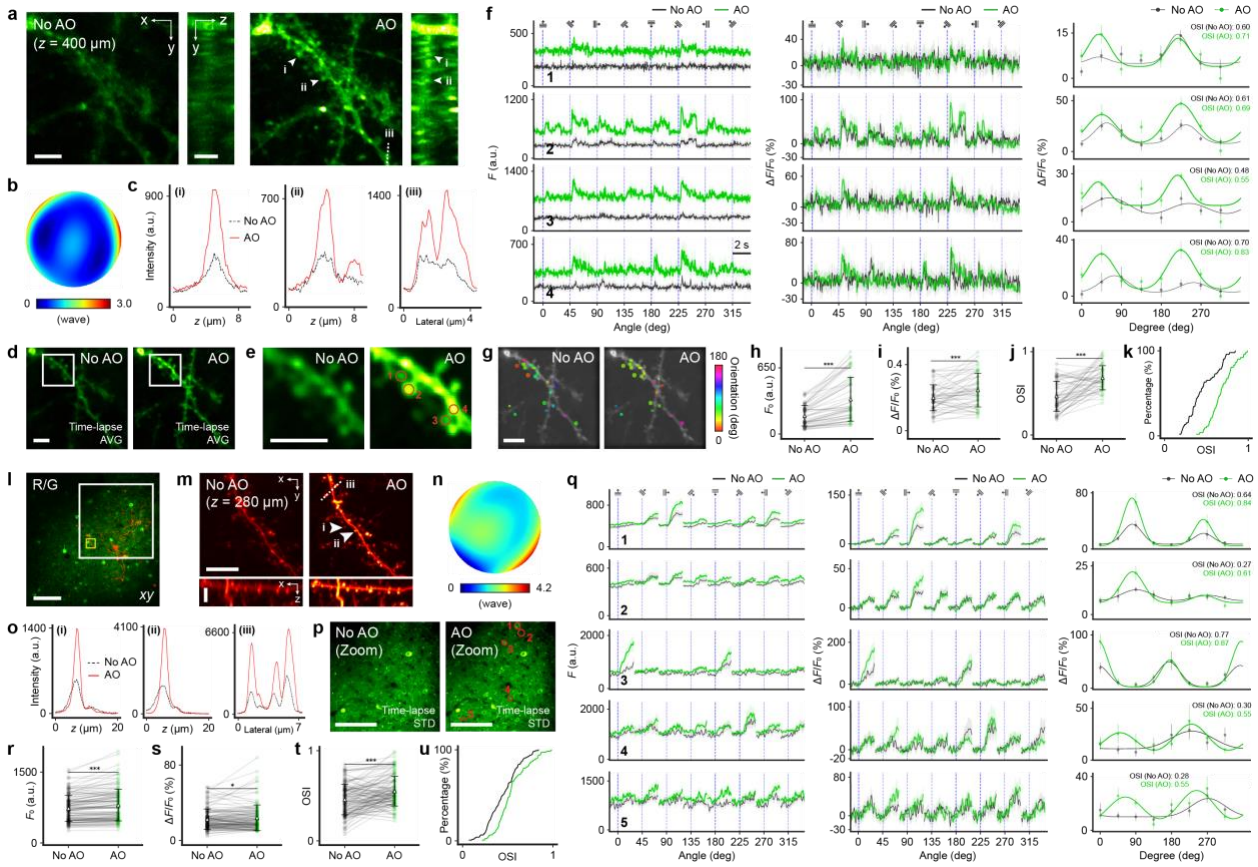

Figure 5. Real-time aberration correction by NeAT for *in vivo* glutamate and calcium imaging. (a) Lateral (*xy*) and axial (*yz*) MIPs of input stacks to NeAT ("No AO") and stacks acquired after aberration correction by NeAT ("AO") of dendrites expressing iGluSnFR3 at 400 µm depth in mouse V1. **(b)** Estimated aberration by NeAT. **(c)** Axial profiles of spines indicated by arrowheads and lateral profiles along dashed line in **a**. **(d)** Average of time-lapse images of dendrites measured without and with AO. **(e)** Zoomed-in views of structures in box in **d**. **(f)** Trial-averaged signal traces (F), glutamate transient traces ($\Delta F/F_0$), orientation tuning curves and OSI values of 4 ROIs (1-4 in **e**). Shade and error bars: s.e.m. **(g)** OS spines in **d** color-coded by their preferred orientations measured without and with AO. **(h-k)** Comparisons of basal fluorescence (F_0; **h**), glutamate transient ($\Delta F/F_0$; **i**), OSIs (**j,k**) of 52 OS spines out of 86 total spines before and after AO correction. Two-sided paired t-test (**h-j**), $p < 0.001$. Kolmogorov-Smirnov test (**k**), $p < 0.001$. **(l)** Superimposed images of sparse tdTomato-expressing neurons (1000-nm excitation) and dense GCaMP6s-expressing neurons (920-nm) at 280 µm depth. **(m)** Lateral (*xy*) and axial (*xz*) MIPs of dendrites (yellow box in **l**) measured without ("No AO", input to NeAT) and with AO. **(n)** Estimated aberration by NeAT. **(o)** Axial profiles for spines indicated by arrowheads and lateral profiles along dashed line in **m**. **(p)** Standard deviation of time-lapse images of GCaMP6s-expressing neurons in white box in **l**, acquired without and with AO. **(q)** Trial-averaged signal traces (F), calcium transient traces ($\Delta F/F_0$), orientation tuning curves, and OSI values of 5 ROIs (1-5 in **p**). Shade and error bars: s.e.m. **(r-u)** Comparisons of basal fluorescence (F_0; **h**), calcium transient ($\Delta F/F_0$; **s**), OSIs (**t,u**) of 125 OS ROIs out of 255 somatic and neuronal structures before and after AO correction. Two-sided paired t-test, $p < 0.001$ (**r,t**), $p < 0.05$ (**s**). Kolmogorov-Smirnov test (**u**), $p < 0.001$. Scale bars: (**a,d,e,g**) 5 µm; (**l,p**) 100 µm; (**m**) 10 µm.

Supplementary Materials

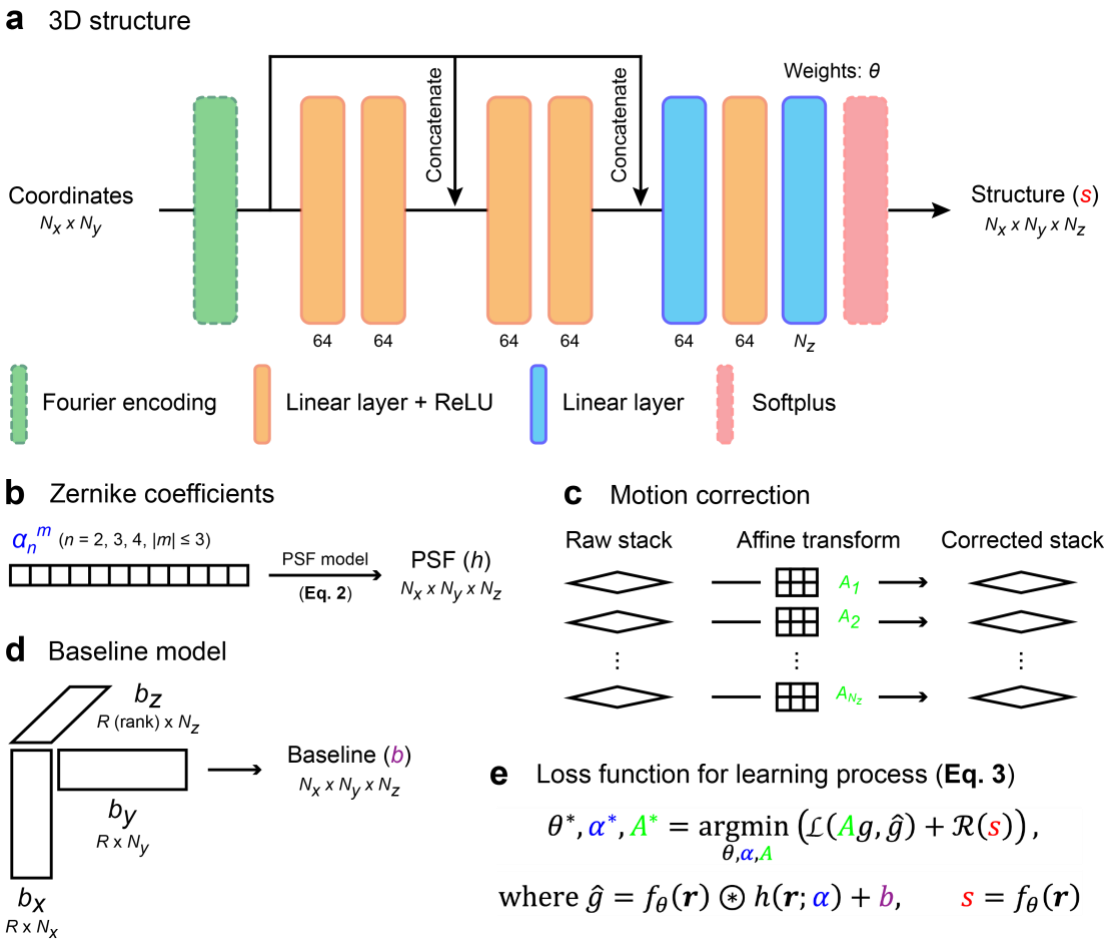

Figure S1. Algorithmic components of NeAT. (a) Structure is represented as a neural field, an implicit function modeled by a coordinate-based neural network that takes spatial coordinates as input and outputs the 3D structure. The numbers below the network layers indicate the number of features per layer. **(b)** Zernike coefficients are represented as a 1D tensor, following the numbering convention of the ANSI standard. **(c)** Motion correction is applied using affine transforms, which are applied to each slice along the z-axis of the raw image stack. **(d)** The baseline term is represented by three 2D tensors, which are combined multiplicatively to generate a low-rank 3D baseline. **(e)** The loss function for the learning process is defined as shown in **Eq. 3**.

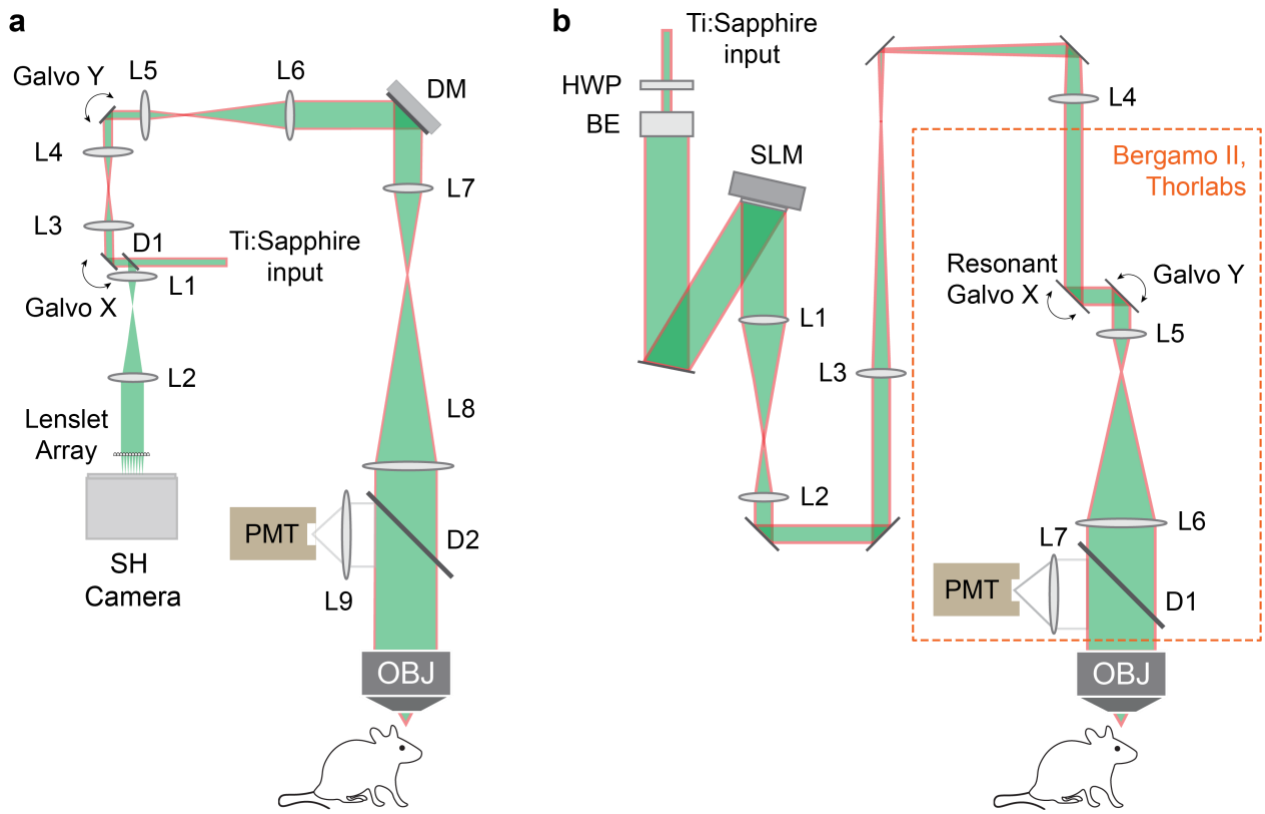

Figure S2. Optical schematics of the custom-built and commercial AO 2P microscopes. (a) Custom-built microscope with a DM perfectly conjugated with Galvo X, Galvo Y, and back focal plane of the objective lens. **(b)** Commercial microscope (Bergamo II, Thorlabs; orange dashed box) with an SLM module and unconjugated galvos.

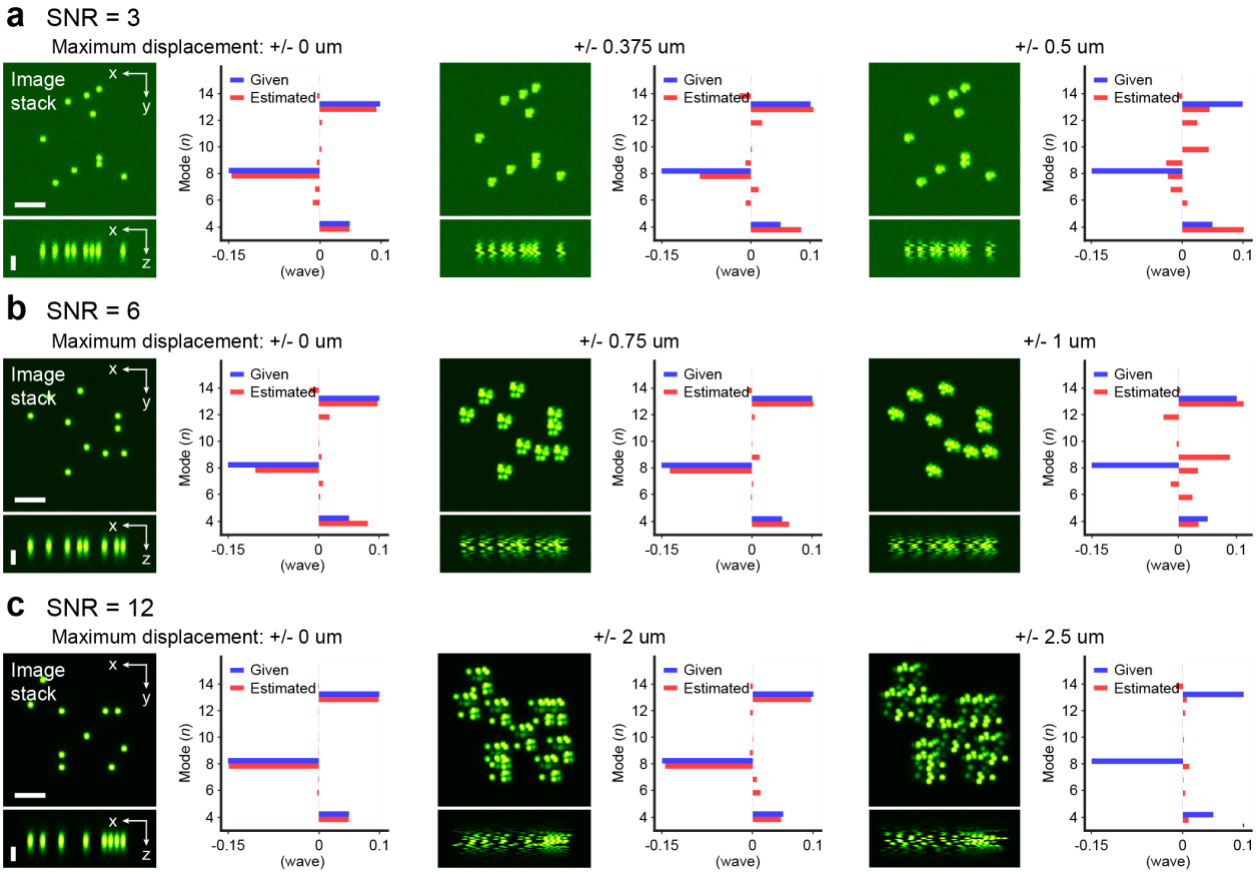

Figure S3. Motion correction performance under different SNRs and maximum displacements. NeAT's motion correction performance on simulated image stacks with an aberration of 0.187 wave RMS is evaluated across varying maximum displacements across different SNRs: SNR = 3 (low SNR, **a**), 6 (intermediate SNR, **b**), and 12 (high SNR, **c**). The results are based on simulated data, where SNR was controlled according to the signal-noise model: $g = P_{\lambda}(\boldsymbol{h} \circledast \boldsymbol{s}) + \boldsymbol{n}$, where $P_{\lambda}(\cdot)$ denotes a Poisson random number generator with a mean of λ, h and s represent the simulated PSF and structure, respectively, and n is a Gaussian random variable. Lateral (*xy*) and axial (*xz*) MIPs of the image stacks are shown. Scale bar: 5 µm.

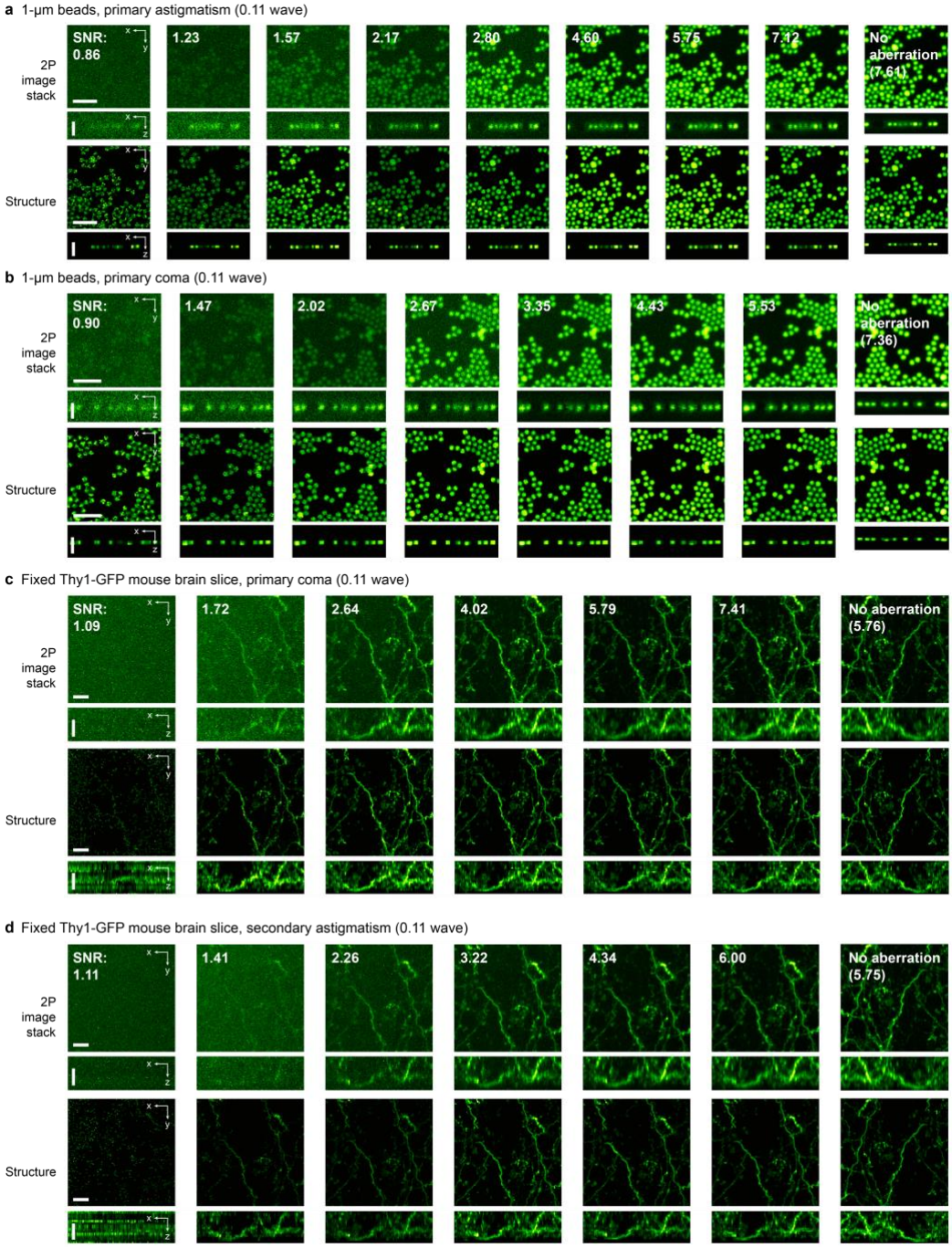

Figure S4. Image stacks and corresponding recovered structures by NeAT for cutoff SNR analysis. **(a)** Lateral (*xy*) MIP and *xz*-slice of input 2P fluorescence image stacks of 1-µm fluorescence beads at varying SNR levels, acquired with primary astigmatism aberration (0.11 wave RMS) applied to the DM after system aberration correction, along with the corresponding structures recovered by NeAT. **(b)** Same as **a** but with primary coma (0.11 wave). **(c,d)** Same as **a,b**, but of image stacks of a fixed Thy1-GFP line M mouse brain slice acquired with primary coma aberration (0.11 wave; **c**) and secondary astigmatism (0.11 wave; **d**). Lateral (*xy*) and axial (*xz*) MIPs of the image stacks, along with the corresponding structures, are shown. Scale bar: 5 µm.

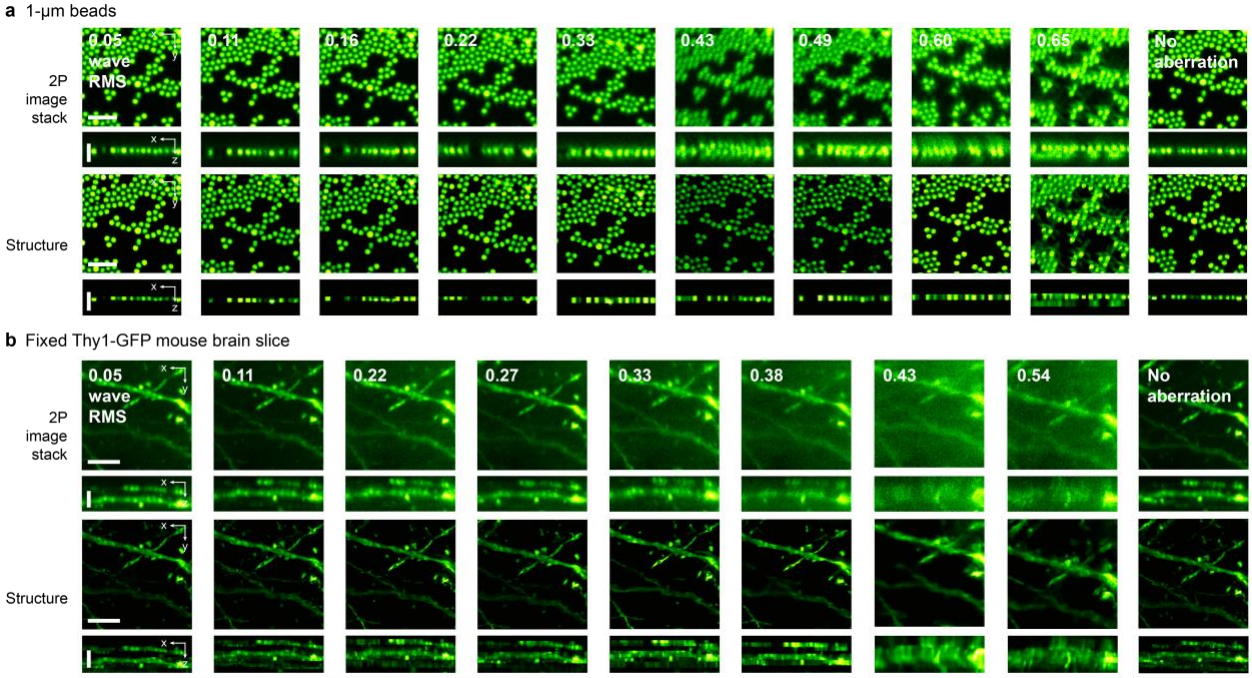

Figure S5. Image stacks and corresponding recovered structures by NeAT for cutoff RMS analysis. **(a)** Lateral (*xy*) MIP and *xz*-slice of input 2P fluorescence image stacks of 1-μm fluorescence beads acquired with randomly generated aberrations of varying aberration severity (in wave RMS) applied to the DM after system aberration correction, along with the corresponding structures recovered by NeAT. **(b)** Same as **a**, but of image stacks of a fixed Thy1-GFP line M mouse brain slice. Lateral (*xy*) and axial (*xz*) MIPs of the image stacks and the corresponding structures are shown. Scale bars: 5 μm.

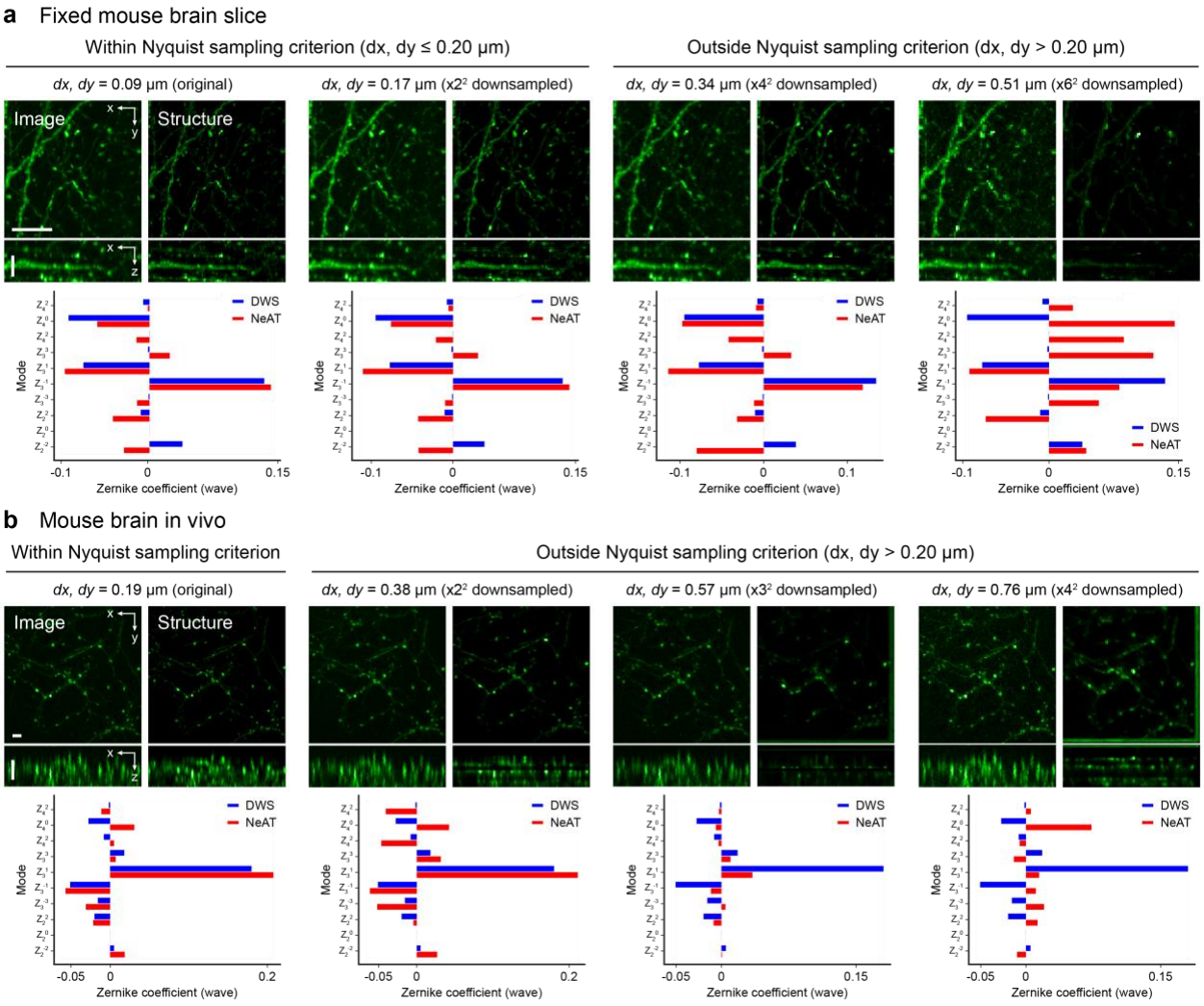

Figure S6. Impact of pixel size and downsampling of image stacks along *x* and *y* axes on NeAT's performance. Lateral (*xy*) and axial (*xz*) MIPs of input image stacks and the corresponding structures, and aberration output by NeAT of a fixed mouse brain slice **(a)** and an *in vivo* mouse brain **(b)** at different pixel sizes (*dx*, *dy*) and downsampling factors along the lateral axes. Zernike coefficients of NeAT output are compared with those from direct wavefront sensing (DWS). Scale bars: **(a)** 10 μm, **(b)** 5 μm.

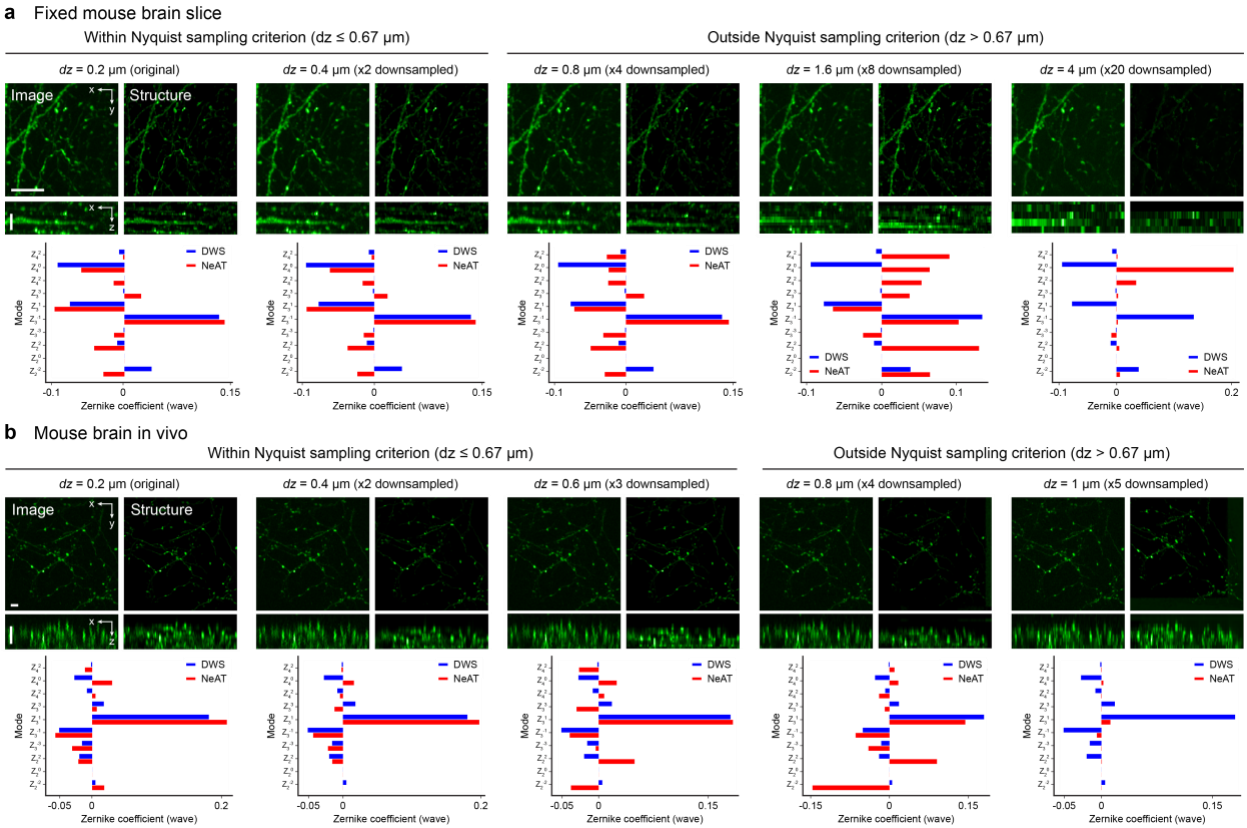

Figure S7. Impact of pixel size and downsampling of image stacks along *z* axis on NeAT's performance. Lateral (*xy*) and axial (*xz*) MIPs of input image stacks and the corresponding structures, and aberration output by NeAT of a fixed mouse brain slice **(a)** and an *in vivo* mouse brain **(b)** at different pixel sizes (*dz*) and downsampling factors along *z* axis. Zernike coefficients of NeAT's output are compared with those from direct wavefront sensing (DWS). Scale bars: **(a)** 10 μm, **(b)** 5 μm.

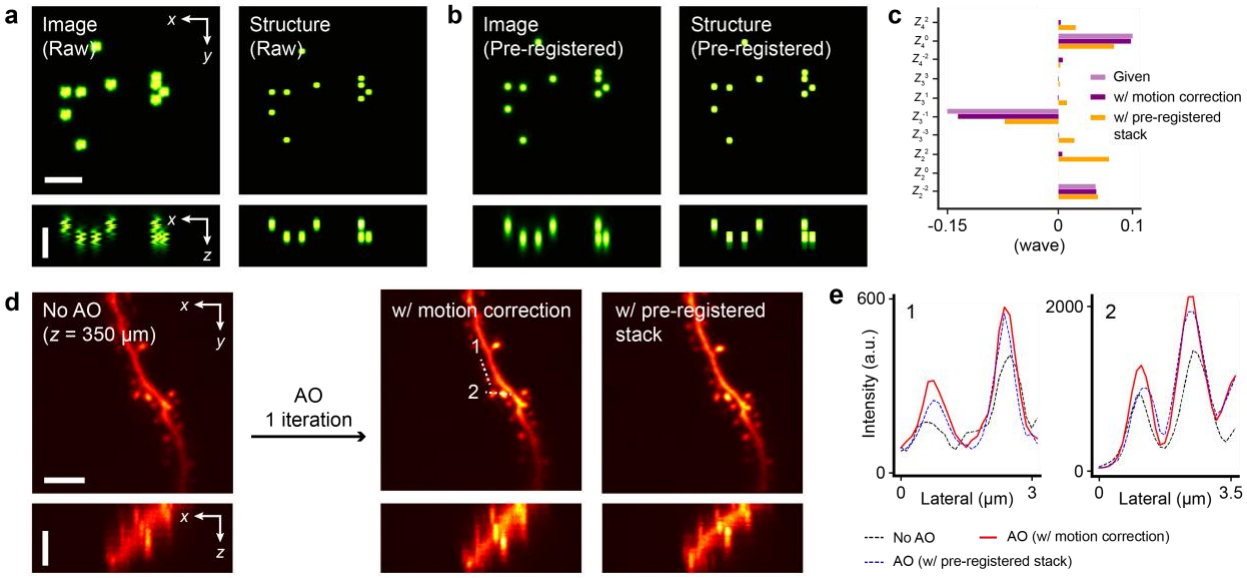

Figure S8. Comparison between motion correction by NeAT and pre-NeAT motion correction by StackReg. (a) Lateral (*xy*) and axial (*xz*) MIPs of the input image stack acquired with an aberration of 0.187 wave RMS and simulated motion artifacts, along with the structure estimated by NeAT using its learnable motion correction procedure. (**b**) Lateral and axial MIPs of the input image stack obtained by pre-registering the input stack in **a** with StackReg ImageJ plugin and the structure estimated by NeAT. **(c)** Zernike coefficients for applied aberration, aberration estimated by NeAT in **a** ('w/ motion correction'), and aberration estimated by NeAT in **b** ('w/ pre-registered stack'). **(d)** Lateral and axial MIPs of image stacks of dendrites acquired *in vivo* without AO, with aberration correction by NeAT with its learnable motion correction procedure, and with aberration correction by NeAT using a pre-registered input stack by StackReg. **(e)** Lateral signal profiles along dashed lines in **d**. Scale bars: 5 μm.

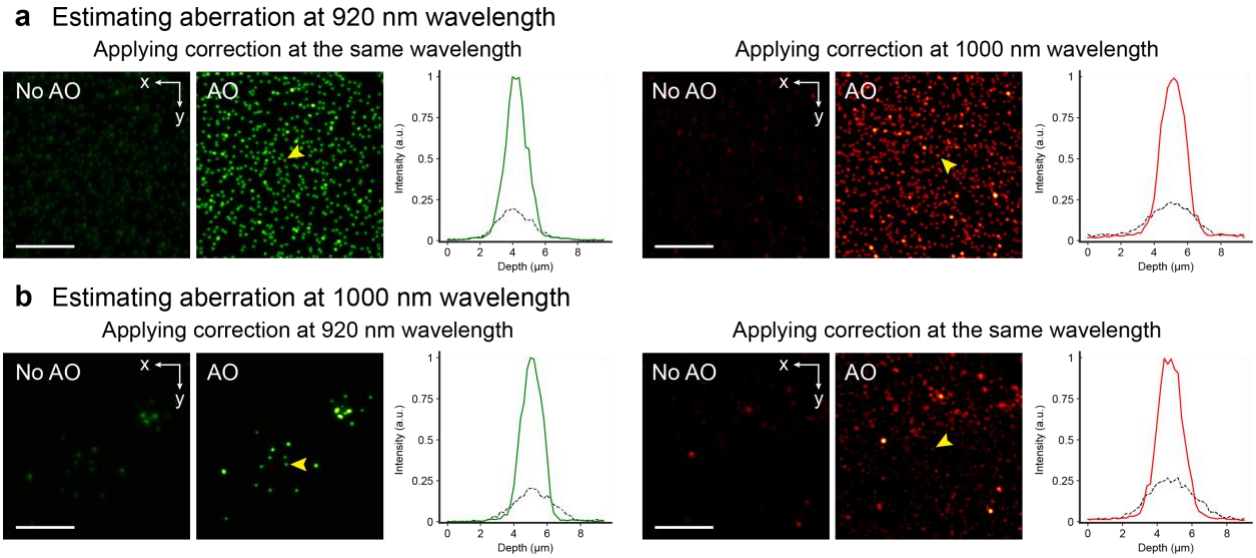

Figure S9. Aberration correction using estimated aberrations at the same or different wavelengths for estimation and correction. (a) Correction at 920 nm and 1000 nm excitation wavelengths, based on aberrations estimated at 920 nm. Lateral (*xy*) MIPs of 200-nm green and red fluorescence beads are shown, with axial intensity profiles compared with and without AO (indicated by yellow arrowheads). (b) Correction at 1000 nm and 920 nm excitation wavelengths, based on aberrations estimated at 1000 nm. Lateral MIPs and axial intensity profiles are compared with and without AO for each case. Scale bars: 10 μm.

Table S1. Differences between NeRF and NeAT.

	NeRF	**NeAT**
Input	A set of 2D images from various viewpoints	A 3D image stack from a single viewpoint
Output	Color, density	Zernike coefficients, structure
Image formation model	Ray tracing for 3D scene reconstruction	Two-photon fluorescence microscopy
Loss function	Mean squared error	Hybrid loss (SSIM, relative MSE)
Application	Computer graphics, virtual reality	*In vivo* imaging with adaptive optics
Additional features	-	Conjugation error correction, motion correction, aberration estimation

Table S2. Experimental settings and estimation time of NeAT.

	Fig. 2a, b	**Fig. 2e-g**	**Fig. 3c**	**Fig. 4a**	**Fig. 4d**	**Fig. 4g**	**Fig. 5a**	**Fig. 5m**
Sample type	Thy1-GFP line M brain slice	Thy1-GFP line M *in vivo*	200-nm fluore-scence beads	C57BL/6J *in vivo* (tdTomato)	Thy1-GFP line M *in vivo*	Thy1-GFP line M *in vivo*	C57BL/6J *in vivo* (iGluSnFR3)	C57BL/6J *in vivo* (tdTomato, GCaMP6s)
Excitation wavelength (nm)	920	920	920	1000	920	920	920	1000
Post-objective power (mW)	4	6	4	21	23	50	72	29
Numerical aperture	1.1	1.1	1.05	1.05	1.05	1.05	1.05	1.05
Input stack size (μm^3)	34.2 × 34.2 × 20	76 × 76 × 10	25 × 25 × 10	25 × 25 × 10	25 × 25 × 10	25 × 25 × 10	28 × 28 × 8	25 × 25 × 10
Pixel size (*dx*, *dy*, *dz*) (μm)	(0.086, 0.086, 0.2)	(0.19, 0.19, 0.2)	(0.125, 0.125, 0.2)	(0.125, 0.125, 0.2)	(0.125, 0.125, 0.2)	(0.125, 0.125, 0.2)	(0.125, 0.125, 0.2)	(0.125, 0.125, 0.2)
Motion correction	No	Yes	No	Yes	Yes	Yes	Yes	Yes
Estimation time (s)	493	436	83	245	245	245	200	245